Materials Advances

ROYAL SOCIETY OF CHEMISTRY

REVIEW

View Article Online
View Journal | View Issue

Cite this: *Mater. Adv.*, 2025, 6, 7207

Transition metal oxide/chalcogenide-integrated MXene heterostructures: emerging materials for supercapacitors and water splitting

Sandra Mathew,[abc] Kalathiparambil Rajendra Pai Sunajadevi *[ac] and Dephan Pinheiro[ac]

The growing global demand for sustainable energy solutions necessitates advancements in energy storage and conversion technologies, aligning with the United Nations' sustainable development goals. MXenes, a novel class of two-dimensional (2D) materials discovered in 2011, have demonstrated immense potential in these fields. Their high surface area, expanded interlayer spacing, metallic conductivity, biocompatibility, abundant redox-active sites, and hydrophilicity make them highly promising for supercapacitors and water-splitting applications. However, MXene layers are prone to agglomeration due to hydrogen bonding and van der Waals interactions, which reduce the active surface area, obscure reaction sites, and hinder ion transport pathways. To overcome these challenges, hybridizing MXenes with transition metal oxides (TMOs) and transition metal chalcogenides (TMCs) can effectively prevent restacking while introducing synergistic functionalities that enhance their overall properties. This review first provides an in-depth discussion on MXene/TMO and MXene/TMC composites for supercapacitors, highlighting their structural advantages and synergistic interactions. It then explores their efficiency in electrocatalytic water splitting, examining their role in enhancing reaction kinetics and overall performance. Finally, the review addresses key challenges, including large-scale synthesis, structural stability, and long-term durability, while offering future research perspectives aimed at optimizing material design, improving performance, and advancing real-world applications in energy storage and conversion.

Received 4th July 2025,
Accepted 5th September 2025

DOI: 10.1039/d5ma00706b

rsc.li/materials-advances

1. Introduction

Global economic growth continues to drive industrial activities, intensifying the depletion of non-renewable energy sources and exacerbating environmental challenges. These pressing challenges have heightened global attention to renewable energy as a critical solution.[1] Today, the role of renewable energy in achieving sustainable development is widely acknowledged, offering cleaner energy solutions that align with environmental and socio-economic goals.

Although renewable energy and sustainable development are distinct concepts, their interdependence is clear. The World Summit on Sustainable Development in Johannesburg in 2002 emphasized the necessity of renewable energy to facilitate a shift toward sustainable consumption and production.[2] Integrating renewable energy into global energy systems not only addresses environmental challenges but also supports broader economic and social advancements, laying a robust foundation for sustainable growth.

The United Nations' sustainable development goals (SDGs) provide a comprehensive framework for addressing critical challenges, including access to clean energy storage and generation (Fig. 1).[3] SDG 7 aims to guarantee universal access to affordable and sustainable clean energy. Transitioning to clean energy is fundamental for achieving sustainability; however, challenges such as inadequate infrastructure and limited investment in renewable energy technologies hinder progress.[4] Prioritizing energy efficiency measures and advancing clean energy solutions are critical for expanding access, particularly in underserved regions.

In the field of energy generation, electrochemical water splitting has emerged as a highly explored area due to its capability to efficiently produce high-purity hydrogen on a large scale with minimal environmental impact.[5] Recent studies on coal and hydrocarbon reserves indicate that current resources

[a] *Department of Chemistry, Christ University, Bengaluru 560029, Karnataka, India. E-mail: sunajadevi.kr@christuniversity.in*
[b] *Department of Chemistry, Mount Carmel College (Autonomous), Bengaluru 560001, Karnataka, India*
[c] *Centre for Renewable Energy and Environmental Sustainability, Christ University, Bangalore-560 029, Karnataka, India*

Fig. 1 Sustainable development goals declared by the United Nations.

may be exhausted within 50–60 years, emphasizing the urgent need to transition to alternative energy sources.[6] Any alternative fuel must avoid the environmental drawbacks associated with carbon-based fuels. In this context, hydrogen has been widely recognized by researchers as a promising solution to address energy-related environmental challenges, offering a pathway towards sustainable energy and a greener planet. Hydrogen is considered a promising "carbon-neutral" energy carrier.[7] The oxygen can be released into the atmosphere, while the hydrogen is stored for future use, where it is oxidized to release energy and form water again.[8,9] Hydrogen possesses several notable benefits, such as low toxicity, safe transportation over long distances through pipelines, and a high energy density per unit mass, which is roughly three times greater than that of gasoline.[10,11]

Along with energy generation, energy storage is another important aspect that requires attention. Supercapacitors represent a modern class of energy storage systems that fill the performance gap between traditional capacitors and batteries.[12] Unlike batteries, which often experience a rapid decline in efficiency with repeated charging cycles, supercapacitors maintain high efficiency and exhibit superior performance. Supercapacitors stand out for their high capacitance, exceptional power density, wide operating temperature range, and long-term durability.[13] Supercapacitors are also integrated into electric and hybrid vehicles, where they provide quick bursts of power for acceleration and regenerative braking systems.[14,15] In consumer electronics, they enable backup power and energy-efficient performance in devices such as laptops, cameras, and wearable technology. Additionally, supercapacitors are utilized in industrial applications like grid stabilization, heavy machinery, and uninterruptible power supplies.[16] Their ability to deliver high power quickly makes them valuable in aerospace, military, and medical devices, where reliability and efficiency are critical.[17] With ongoing advancements in materials and design, supercapacitors continue to expand their role in modern energy storage and management solutions.

MXenes, a cutting-edge class of two-dimensional materials, play a pivotal role in advancing energy generation and storage. Their exceptional properties enable their effective utilization in electrochemical water splitting and supercapacitors.[18,19] Furthermore, their integration with metal oxides, sulfides, selenides, and other carbonaceous materials enhances their potential, expanding their applicability in sustainable technologies. By leveraging these advancements, MXenes offer innovative pathways toward achieving the Sustainable Development Goals (SDGs), contributing to a cleaner and more sustainable future for all.

2. MXenes and transition metal dichalcogenides/oxides

MXenes constitute a significant family of two-dimensional (2D) materials, consisting of transition metal carbides, nitrides, or

carbonitrides. Their general formula is $M_{n+1}X_nT_x$, where $n + 1$ represents the number of transition metal (M) layers from groups 3 to 6, interleaved with n layers of carbon and/or nitrogen (denoted as X).[20,21] The outermost M layers are functionalized with surface terminations, designated as T_x, which may include F, O, or OH. Within the MXene structure, X atoms occupy octahedral interstitial sites within the hexagonal sublattice of M layers, while surface functional groups attach at various locations on these metal layers.[22,23] MXenes are typically synthesized by selectively removing the 'A' layer from their parent MAX phases, where the 'A' element belongs to groups 13 or 14 (Fig. 2). MXenes stand out due to their outstanding electrochemical properties, surpassing conventional carbon-based materials in features such as electrical conductivity, ease of processing, thermal stability, metallic conductivity, surface chemistry, and high surface area. The core transition metal carbide structure is the key to their remarkable electrical conductivity, enabling excellent charge transfer throughout the electrocatalytic processes.[24] The ultrathin layered morphology of MXenes provides a high specific surface area, exposing numerous active sites that accelerate reaction kinetics. Another crucial characteristic is their hydrophilicity, which facilitates easy access of reactants to active sites and enhances charge carrier transport, thereby improving the performance. Moreover, their excellent corrosion resistance and stability under harsh conditions make them a robust choice as a support material for electrocatalytic applications. These exceptional attributes position MXenes as promising candidates as electrocatalysis.[25]

However, the practical application of MXenes in electrochemical systems faces several challenges. One significant issue is the tendency of MXene layers to restack, reducing their accessible surface area and limiting their electrochemical performance. Additionally, freshly synthesized MXenes are highly susceptible to oxidation, which further diminishes their electrocatalytic activity. Studies also show that MXenes exhibit poor stability in aqueous electrolytes and suffer from low cycling durability.[27]

Combining various electrocatalysts with MXenes prevents layer agglomeration and thereby enhancing electrocatalytic performance. The functional groups on the MXene surface facilitate strong chemical bonding and uniform distribution of electrocatalysts. Hetero structuring MXenes with different electrocatalysts presents new research possibilities and can further enhance their electrocatalytic efficiency.[28] Additionally, incorporating nanocarbon, conductive polymers, heteroatoms, transition metal oxides (TMOs), and transition metal dichalcogenides (TMDs) significantly increases interlayer spacing, leading to improved electrochemical performances.

TMDs and TMOs exhibit excellent electrocatalytic properties, including high surface area, good electrical properties, atomically thin layers, and stability.[29] However, TMDs suffer from poor cycling stability, low conductivity, and limited active sites,[30,31] while TMOs tend to agglomerate, restricting their performance.[32–34] Recent studies highlight that combining these materials with MXenes leverages both strengths. Integrating MXenes with these materials prevents layer restacking, enhancing

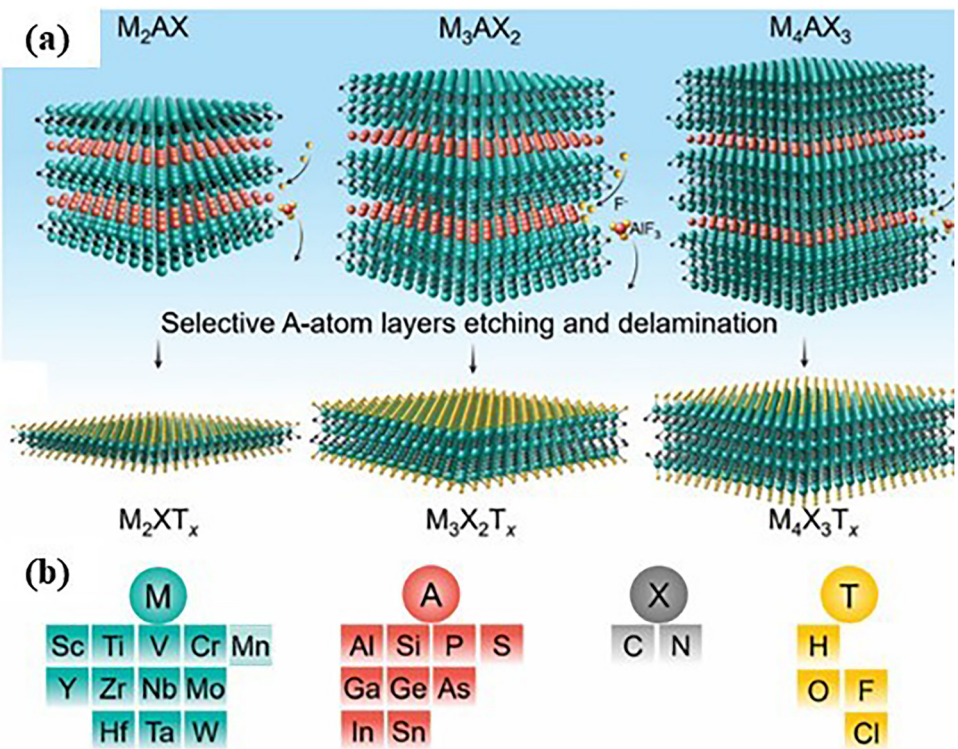

Fig. 2 (a) Schematic illustration of synthesizing different MXenes from their precursor MAX phases (b) Possible elements for M, A, X, and T in MAX phases and MXene. Reproduced with permission from ref. 26 copyright 2012, Elsevier.

the contact area between the electrolyte and electrode.[35] Additionally, the 2D heterointerface features van der Waals interactions that mitigate Fermi-level pinning. This, combined with the work function tunability of metallic MXenes, enables Schottky barrier-free contact and reduces contact resistance. As a result, these composites exhibit excellent reversible specific capacitance, superior coulombic efficiency, and enhanced cyclability and rate performance in electrochemical applications.[36]

The surface chemistry of MXenes, primarily governed by functional groups such as –O, –OH, and –F, plays a decisive role in the nucleation, growth, and overall architecture of MXene-based composites. These terminations strongly influence surface charge, hydrophilicity, interlayer spacing, and chemical reactivity, which together determine the efficiency of incorporating transition metal oxides/carbides and other secondary phases into the MXene matrix.[36] Among these groups, –O and –OH terminations provide abundant active sites for coordination with transition metal cations, facilitating uniform nucleation and the formation of strong interfacial bonds (*e.g.*, Ti–O–M linkages) that stabilize the composite structure.[37] Their negative surface charge in aqueous media further promotes electrostatic interactions with positively charged precursor species, enabling homogeneous dispersion and layer-by-layer assembly of nanoparticles or polymers.[37,38] Additionally, the hydrophilic nature of –O and –OH enhances wettability, allowing electrolyte penetration and precursor accessibility, which is crucial for achieving dense and conformal deposition of active materials.[39] In contrast, –F terminations are relatively inert and reduce the density of anchoring sites available for composite formation. Post-treatment strategies, such as alkalization and thermal annealing, are therefore frequently employed to reduce –F content and enrich the surface with –OH or –O groups, leading to improved compatibility and stronger interfacial integration.[40]

Furthermore, functional groups influence the interlayer spacing of MXenes during composite synthesis. Hydrogen bonding between –OH/–O terminations and intercalated molecules or ions can effectively expand the layer distance, preventing MXene restacking and enabling higher accommodation of TMO/TMC nanoparticles within the layered structure.[41] This expanded spacing not only improves mass loading but also facilitates efficient ion diffusion pathways within the composite.[41]

The synergistic interaction between conductive MXenes and high-capacity TMDs/TMOs makes these heterostructures highly promising electrode materials for supercapacitors.

3. MXene-based composites for supercapacitance studies

MXenes have gained considerable interest for their promising applications in energy storage, especially in supercapacitors. When combined with transition metal oxides and transition metal chalcogenides, MXenes form advanced composites that leverage the strengths of both material classes.

3.1. MXene/transition metal oxide composites for supercapacitance studies

MXene/transition metal oxide (TMO) composites have emerged as promising candidates for high-performance supercapacitors due to their synergistic electrochemical behaviour. The conductive and layered structure of MXenes offers rapid electron transport and high surface area, while TMOs contribute substantial pseudocapacitance through redox reactions. This combination effectively enhances specific capacitance, energy density, and cycling stability. These hybrid materials demonstrate excellent rate capability and long-term durability, making them ideal for next-generation energy storage devices.

3.1.1. MXene/manganese oxide composites. Among all the transition metal oxides, MnO_2 sets itself apart as an extremely effective material for energy storage devices. This distinction arises from its high theoretical specific capacitance, rapid charge–discharge ability, wide potential window, and low corrosiveness to the current collector in alkaline media.[37,42] Compared to other transition metal oxides, MnO_2 offers advantages in cost-effectiveness, ease of fabrication, low toxicity, and environment friendliness.[38,43,44] MnO_2 exists in six distinct crystal phases (α, β, γ, δ, ε, and λ), each contributing to a diverse range of structural forms.[45] Despite these benefits, MnO_2-based materials experience drawbacks like reduced capacitance and shortened cycling life, which are attributed to low electronic conductivity, easy agglomeration, and Mn dissolution during redox reactions.[46,47] The combination of MnO_2 with MXenes is extensively studied due to its favorable electrochemical properties, which improve the efficiency of MXene-based composites in various energy storage techniques.

MXene/MnO_2 composites with diverse morphologies were synthesized using various methods, including hydrothermal, electrostatic self-assembly, electrodispersion, ultrasonication, and solvothermal techniques. Wang *et al.* have synthesized MXene/MnO_2 composite *via* the hydrothermal method, and it showed a specific capacitance (C_{sp}) of 242 F g^{-1} with a capacitance retention of 97% over 5000 cycles.[48] The suboptimal performance of the MXene/MnO_2 composite may stem from the agglomeration of MnO_2 particles on the MXene surface, as evidenced by SEM images. This aggregation indicates that MnO_2 nanoparticles are unevenly distributed, limiting the accessibility of ions across the composite and reducing the effectiveness of electrochemical reactions. Additionally, the surface area of the composite was insufficient to support enhanced performance, as higher surface areas are critical for maximizing active sites and facilitating efficient ion diffusion. In a similar study, Yuan *et al.* employed a similar hydrothermal strategy but optimized the synthesis conditions, resulting in a Ti_3C_2/MnO_2 composite with a much higher specific surface area of 88.6 m^2 g^{-1} compared to the 26.05 m^2 g^{-1} reported in the previous study.[49] The composite also exhibited abundant micropores and mesopores, which facilitated efficient ion diffusion and provided more active sites. Consequently, this

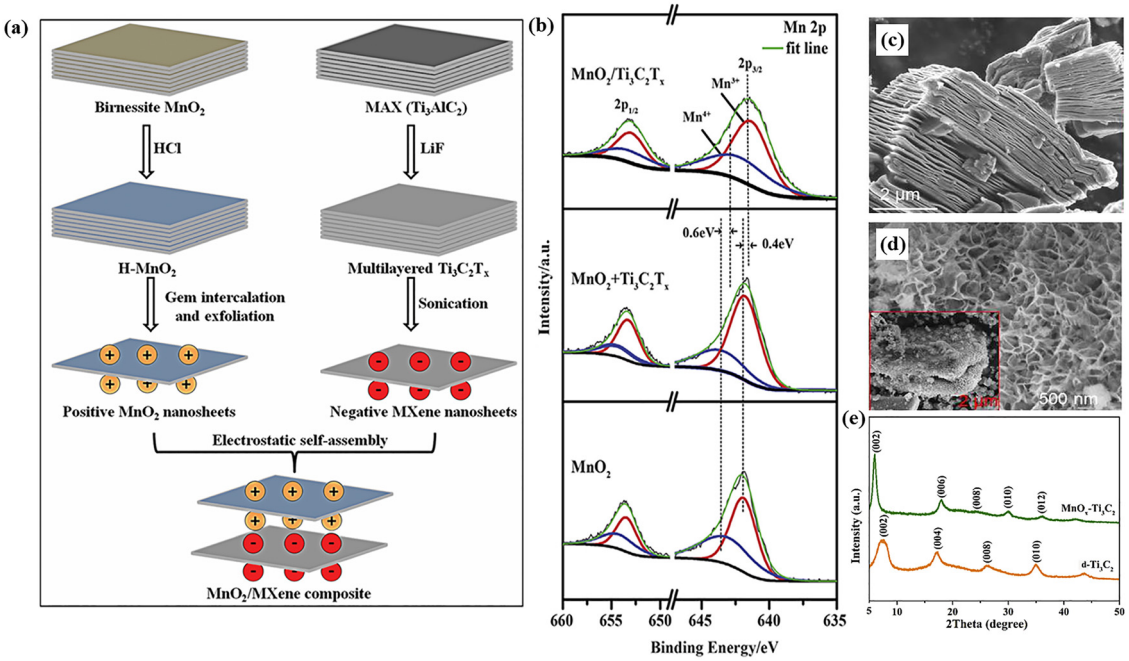

Fig. 3 (a) synthesis of Ti_3C_2/MnO_2. Reproduced with permission from ref. 50 copyright 2019, Royal society of chemistry. (b) XPS analysis of Ti_3C_2/MnO_2. Reproduced with permission from ref. 38 copyright 2018, Elsevier. (c) and (d) SEM analysis of Ti_3C_2 and Ti_3C_2/MnO_2. Reproduced with permission from ref. 52 copyright 2016, American Chemical Society. (e) XRD analysis of d-Ti_3C_2 and Ti_3C_2–MnO_2. Reproduced with permission from ref. 37 copyright 2017, Elsevier.

optimized material achieved an improved C_{sp} of 254 F g^{-1} at a current density of 0.5 A g^{-1} with 97% retention after 5000 cycles. Thus, while the hydrothermal route initially showed limitations due to particle agglomeration and low surface area, careful optimization can overcome these drawbacks, yielding Ti_3C_2/MnO_2 composites with superior capacitive performance.

In 2019, Chen *et al.* designed a Ti_3C_2/MnO_2 composite through electrostatic self-assembly, where negatively charged MXene sheets were decorated with positively charged MnO_2 particles, as schematically shown in Fig. 3a.[50] This mild yet efficient strategy suppresses the agglomeration of MnO_2 and MXene layers, thereby facilitating ion diffusion and improving electrolyte accessibility to the active sites, which in turn enhances the specific capacitance and stability of the electrode. As a result, the MnO_2/MXene composite achieves a high capacitance of 340 F g^{-1}, nearly 2.5 times higher than MnO_2 nanosheets (137 F g^{-1}) and about three times greater than pristine MXene (109 F g^{-1}) at 1 A g^{-1}.

There is a growing demand for energy storage devices, particularly those that are flexible, highly efficient, lightweight, and compact, for use in next-generation portable electronics. Recently, substantial efforts have been directed towards identifying high-performance electrode materials for flexible supercapacitors. Zhou *et al.* designed $Ti_3C_2T_x/MnO_2$ nanowires composite paper with high areal and volumetric capacitance.[51] The ultralong MnO_2 nanowires provide excellent mechanical flexibility to the composite films and function as interlayer spacers between the conductive $Ti_3C_2T_x$ layers, which enhances the exposure of both the inner and outer active surfaces resulting in improved energy storage. Meanwhile, a group of scientists under Jiang has synthesized $Ti_3C_2T_x/MnO_2$ nanoneedles *via* a mild chemical deposition method and tested its supercapacitive behavior in 1 M Na_2SO_4.[38] XPS analysis (Fig. 3b), reveals charge transfer from the MXene layers to the MnO_2 nanoneedles, with the MXene layers serving as an excellent conductive matrix that facilitates electron transfer within the nanocomposites. The efficient synergistic interaction between MnO_2 and MXene, driven by chemical interactions, significantly enhances the conductivity, C_{sp}, and stability of the composite. In another study, Rakhi and coworkers introduced a novel method for synthesizing Ti_3C_2/MnO_2 through direct chemical synthesis.[52] The ε-MnO_2 nanowhiskers significantly enhance the electrode's surface area, leading to a threefold improvement in C_{sp} value compared to the pristine MXene-based symmetric supercapacitor, while also demonstrating long cyclic life. Additionally, the open porous morphology (Fig. 3c and d) of ε-MnO_2 on MXene sheets promotes rapid ion diffusion and facilitates improved redox reactions, further enhancing supercapacitor performance when used as electrode materials in aqueous supercapacitors.

In another study, flexible and free-standing MnO_2–Ti_3C_2 films were synthesized using a facile *in situ* wet chemistry method.[37] The XRD spectrum illustrated in Fig. 3e reveals an increase in the interlayer spacing of MXene layers after the intercalation of MnO_2 particles, which enhances the availability of active sites. The energy storage performance of the flexible electrodes was evaluated through various electrochemical tests, showing an impressive volumetric capacitance of 602 F cm^{-3} at 2 mV s^{-1}, a low internal resistance of 5.4 Ω, and capacitance retention of 89.8% after 10 000 cycles. Zhou *et al.* developed a highly flexible and conductive MnO_2/MXene/carbon cloth

freestanding electrode using a one-pot hydrothermal method.[43] Due to the synergistic interaction between α-MnO_2 nanorods and Ti_3C_2 layers, the composite achieved a high C_{sp} of 511.2 F g^{-1}, significantly outperforming pristine electrodes. Additionally, the modified composite displayed lower resistance parameters, attributed to the formation of an efficient conductive network within the structure.

Liu *et al.* have designed a multicomponent flexible electrode by distributing MnO_2 nanorods over MXene layers hydrothermally and coating them over carbon nanotube fibres.[53] The electrode demonstrates a C_{sp} of 181.8 F g^{-1} and excellent durability. Additionally, the fibrous electrodes maintain stable electrochemical performance even when bent at angles up to 180°, showcasing their robust flexibility. Li and his team developed another multicomponent system by electrodepositing MnO_2 and CoNi layered double hydroxides onto a carbon cloth/MXene electrode.[54] The nanoarray morphology provides a high surface area and additional charge transfer channels, enabling rapid ion and electron diffusion between the electrolyte and electrode. They studied the impact of various Co and Ni ratios on electrochemical performance, finding that a Co : Ni ratio of 1 : 2 yielded the highest C_{sp} of 922 F g^{-1} at 1 A g^{-1}. Mn_3O_4 is another form of manganese oxide widely used in supercapacitor applications. Oyedotun *et al.* prepared a Ti_3C_2/Mn_3O_4 nanocomposite *via* the solvothermal method.[55] The fabricated asymmetric device exhibited an energy density of 28.3 Wh kg^{-1} and a power density of 463.4 W kg^{-1}, with 92.6% capacitance retention over 10 000 cycles.

3.1.2. MXene/iron oxide composites. α-Fe_2O_3 is recognized as a promising electrode among pseudocapacitive materials for supercapacitors, due to its excellent redox activity, broad potential window, natural abundance, environmental compatibility, and cost-effectiveness.[56,57] Through the reversible redox reaction between Fe^{3+} and Fe^{2+}, α-Fe_2O_3 can achieve a theoretical specific capacitance of up to 3625 F g^{-1}. However, the applicability of Fe_2O_3 is constrained by its low electrical conductivity ($\sim 10^{-14}$ S cm^{-1}), resulting in significant charge transfer resistance between the electrode and electrolyte.[58] To address the limitation of low conductivity in Fe_2O_3, extensive efforts have focused on developing Fe_2O_3-based nanocomposite electrodes that enhance conductivity and reduce charge carrier diffusion length. MXene, with its abundance of terminal functional groups, provides an ideal partner for this purpose, as it readily bonds with metal oxides through electrostatic interactions. Thus, designing composite materials that incorporate Fe_2O_3 structure with MXene is essential. This approach not only improves the conductivity of Fe_2O_3 but also prevents the undesirable aggregation of MXene sheets, resulting in a more efficient and stable electrode material. Zou *et al.* developed a $Ti_3C_2T_x$/α-Fe_2O_3 nanocomposite *via* electrostatic self-assembly, marking the first reported use of this electrode material for supercapacitor applications.[59] Positively charged cocoa-like Fe_2O_3 particles were electrostatically attracted to the negatively charged MXene layers, effectively mitigating the restacking of the MXene sheets. The resulting electrode achieved a C_{sp} of 405.4 F g^{-1} within a wide potential window of 0–1.2 V (Fig. 4a) and demonstrated excellent cycling stability with 97.7% capacitance retention over 2000 cycles (Fig. 4b). The suboptimal performance of the synthesized composite could be attributed to the high contact resistance between the MXene nanoparticles and the cocoa-like Fe_2O_3.

Shi *et al.* integrated urchin-like 3D Fe_2O_3 with MXene layers, where the close contact between them significantly enhances conductivity, facilitates charge transfer, and accelerates the redox reactions during the energy storage process.[60] The fabricated asymmetric device, with Fe_2O_3/MXene composite as the anode and MnO_2 as the cathode, exhibited high energy and power densities of 32.2 Wh kg^{-1} and 900.6 W kg^{-1}, respectively, along with excellent capacitive retention. Meanwhile, Ma *et al.* developed a flexible Fe_2O_3NPs@MX electrode through electrostatic self-assembly followed by annealing, which demonstrates a high C_{sp} of 584 F g^{-1}, outperforming both pristine MXene and Fe_2O_3.[61] In this structure, Fe_2O_3 acts as interlayer spacers, while the continuous MXene layers help mitigate the volume expansion of Fe_2O_3 nanoparticles during the charge–discharge cycles. Li *et al.* fabricated a sandwich-type MXene/Fe_3O_4/MXene electrode through a laser crystallization method (Fig. 4c), which showed an enhanced aerial capacitance of 46.4 mF cm^{-2} compared to the $Ti_3C_2T_x$ electrode at 0.5 mA cm^{-2}.[62] Additionally, the assembled symmetric device demonstrated an energy density of 0.970 μWh cm^{-2} at a power density of 0.176 mW cm^{-2}. Liang *et al.* synthesized a $Ti_3C_2T_X$-Fe_3O_4-CNT composite, which exhibited a combination of double-layer capacitive and battery-type properties with a predominantly battery-type charge storage mechanism.[63] Arun and his co-workers synthesized a Fe_3O_4/MXene/rGO composite with a surface area of 57 m^2 g^{-1}, showing a C_{sp} value of 42.8 F g^{-1} at a scan rate of 5 mV s^{-1}.[64] This electrode exhibited an R_{ct} value of 4.42 Ω, and a capacitive retention of 82.1% over 5000 cycles. Ishan *et al.* incorporated silver-doped Fe_2O_3 nanospheres into MXene hydrogel through co-precipitation and ultrasonication methods, achieving a C_{sp} of 709.4 F g^{-1} at 1 A g^{-1}.[65]

3.1.3. MXene/nickel oxide composites. Apart from manganese and iron-based oxides, nickel oxide (NiO) also exhibits remarkable capacitance performance, driven by its efficient redox activity, affordability, and impressive theoretical capacitance.[66] NiO possess a high theoretical capacitance of 2584 F g^{-1}, and also facilitates effective ion insertion and extraction due to its reversible oxidation states.[66] Nevertheless, its limited electronic conductivity leads to poor reaction kinetics, thereby constraining both cycling stability and overall performance.[67] In 2017, Xia and his team focused on asymmetric supercapacitors (ASC) and successfully developed a high-performance electrode by growing NiO nanosheets on a carbon-supported TiO_2 layer derived from MXene (Ni-dMXNC) through a thermal annealing process.[68] The ASC device, fabricated using Ni-dMXNC as the cathode and MXene as the anode, exhibited high energy and power densities of 0.0104 Wh cm^{-3} and 0.22 W cm^{-3}, respectively, with a capacitance retention of 72.1% after 5000 cycles. The improved charge storage efficiency is ascribed to the formation of high surface area multilayer structures within the Ni-dMXNC, the active surface properties of the NiO layer, and the synergistic interaction with the $Ti_3C_2T_x$ MXene as the negative electrode. Zhang *et al.* introduced a vacuum freeze-drying method for the direct chemical

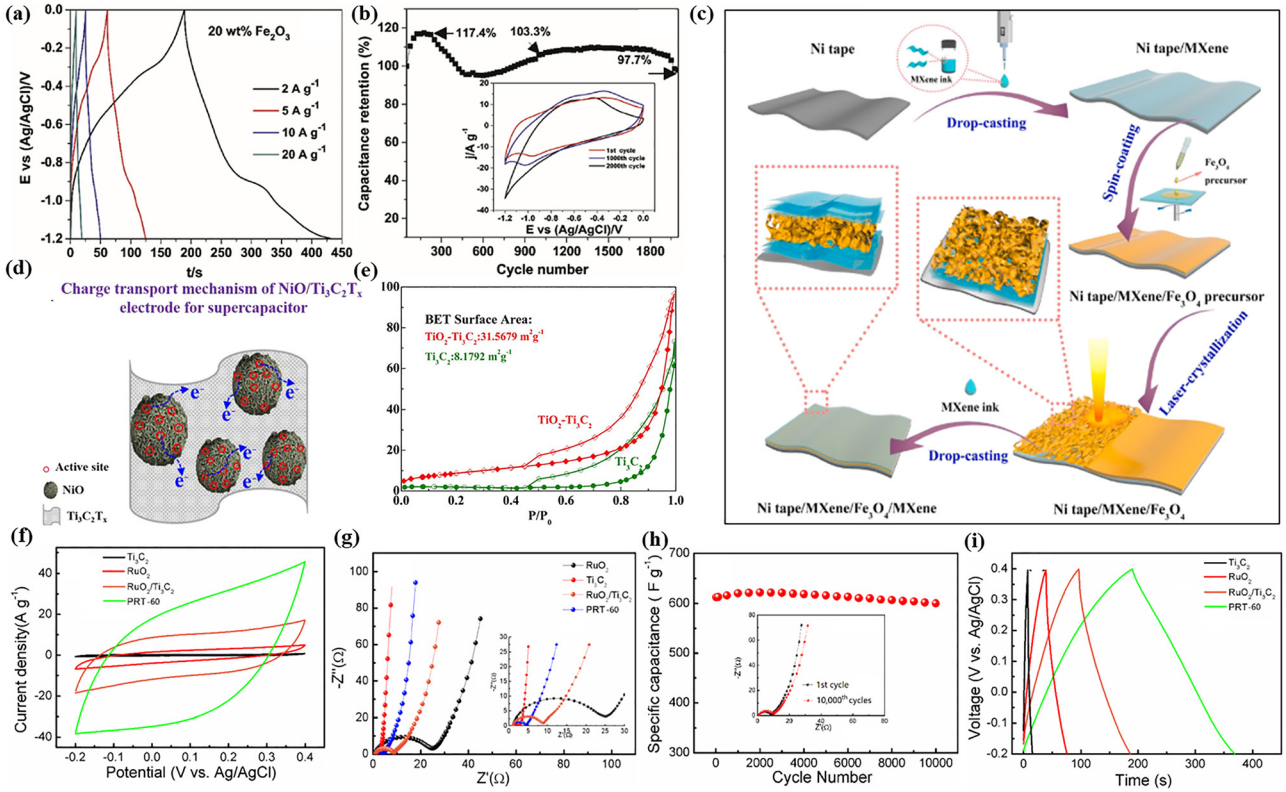

Fig. 4 (a) GCD curve of $Ti_3C_2T_x$/α-Fe_2O_3. Reproduced with permission from ref. 59 copyright 2018, Elsevier. (b) Stability test of $Ti_3C_2T_x$/α-Fe_2O_3[59] copyright 2018, Elsevier. (c) synthesis of MXene/Fe_3O_4/MXene. Reproduced with permission from ref. 62 copyright 2021, Elsevier. (d) Mechanism of charge transport in NiO/$Ti_3C_2T_x$. Reproduced with permission from ref. 67 copyright 2019, Elsevier. (e) surface area comparison of Ti_3C_2 and TiO_2–Ti_3C_2. Reproduced with permission from ref. 70 copyright 2021, Elsevier. Electrochemical analysis of Ti_3C_2, RuO_2/Ti_3C_2, and PRT-60. Reproduced with permission from ref. 71 copyright 2018, MDPI. (f) CV curves (g) GCD curves (h) Nyquist plots (i) stability test of PRT-60.

deposition of NiO onto $Ti_3C_2T_x$.[69] This process led to the formation of 3D porous conductive networks by interconnecting monolayer $Ti_3C_2T_x$, with NiO nanoparticles uniformly distributed on their surfaces. By effectively leveraging the advantages of both materials, such as high surface area and excellent capacitance, the $Ti_3C_2T_x$/NiO composite achieved a high volumetric capacitance of 341 F cm^{-3} at a scan rate of 2 mV s^{-1}. In another study NiO/$Ti_3C_2T_x$ were derived from Ni-MOF/$Ti_3C_2T_x$ through calcination and it showed a battery-type behaviour with enhanced specific capacity of 630.9 C g^{-1} at 1 A g^{-1}.[67] Here, as shown in Fig. 4d, the $Ti_3C_2T_x$ MXene surface decorated with NiO microspheres provides stability and enhances electron transport compared to pristine NiO.

3.1.4. MXene/titanium oxide composites. Integrating MXene with TiO_2 can significantly enhance charge transfer efficiency and improve the structural stability of the hybrid system. Zhu *et al.* synthesized MXene decorated with TiO_2 *via in situ* hydrolysis followed by heat-treatment process.[70] The resulting TiO_2/Ti_3C_2 composite exhibited a surface area approximately four times larger than that of pristine MXene (Fig. 4e). This enhancement was attributed to the reduced restacking of MXene layers, which exposed additional reaction sites and consequently improved its supercapacitive performance.

Recently, Yu *et al.* synthesized a nitrogen-doped porous MXene/TiO_2 flexible electrode using a controlled hydrothermal method.[72] The partial oxidation of MXene resulted in a porous MXene/TiO_2 heterostructure with an enlarged surface area, well-anchored TiO_2 nanoparticles, high electrochemical activity, and excellent capacitive retention. Furthermore, nitrogen doping in the MXene lattice expanded the interlayer spacing, significantly enhancing the material's energy storage performance. The electrode achieved an impressive specific capacitance of 2194.33 mFm^{-2} with a high retention rate of 74.39% after 10 000 cycles. In a related study, Lu *et al.* integrated PANI into $TiO_2/Ti_3C_2T_x$ composite, and achieved enhanced capacitive performance due to the hierarchical structure and synergistic effects among the components.[73]

3.1.5. MXene/ruthenium oxide composites. In addition to the mentioned metal oxides, RuO_2 has also been studied in MXene-based composites for energy storage due to its high theoretical capacitance, electrical conductivity, favorable redox reactions, high thermal stability, and wide operating voltage range.[74,75] However, challenges such as self-aggregation, chemical instability in acidic electrolytes, and high cost hinder its application in supercapacitors.[76,77] Li *et al.* developed a simple *in situ* method to anchor RuO_2 particles onto MXene sheets, which were then combined with silver nanowires (AgNWs) to fabricate a printable electrode for high-performance micro-supercapacitors.[78] In this electrode, RuO_2 delivers high pseudo capacitance and prevents MXene nanosheets from self-stacking, maintaining an efficient ion

transport pathway. Meanwhile, the AgNWs complement the RuO_2@MXene by enhancing the rheological properties of the electrode ink and forming a highly conductive network for fast charge transfer. These micro-supercapacitors demonstrated a high volumetric capacitance of 864.2 F cm^{-3} at 1 mV s^{-1}, exceptional cycling stability with 90% retention over 10 000 cycles. It also delivered high energy and power densities of 13.5 mWh cm^{-3} and 48.5 W cm^{-3}, respectively.

In another study, Zhao *et al.* developed a phosphate ion-modified RuO_2/Ti_3C_2 (PRT) composite using chemical solution synthesis followed by annealing.[71] The Ti_3C_2 layers enhance conductivity, while phosphate ion doping increases the number of active reaction sites. Electrochemical tests (Fig. 4f–i) revealed that PRT achieved a high specific capacitance of 612.72 F g^{-1}, exhibited low resistance parameters, and retained 97.95% of its capacitance after 10 000 cycles.

3.1.6. Other MXene/TMO composites. Cobalt, vanadium, and tungsten-based metal oxides were also incorporated with MXenes for energy storage applications. Liu *et al.* synthesized a Co_3O_4-doped 3D MXene/RGO aerogel *via* a freeze-drying method. Co_3O_4 nanoparticles were first chemically deposited onto $Ti_3C_2T_x$ layers through $CoCl_2$ reduction and then freeze-dried.[79] The resulting Co_3O_4-MXene was mixed with GO dispersions in varying ratios, freeze-dried again, and thermally annealed to synthesize Co_3O_4-MXene/RGO (CMR) aerogel. The remarkable capacitance of 345 F g^{-1} exhibited by the CMR hybrid porous aerogel electrodes can be attributed to their unique structural design. The enhanced surface area and porous nature provide abundant reaction sites, shorten the electrolyte ion diffusion distance, and accelerate electron transport during charge–discharge cycles, while the layered MXene structure ensures stability by preventing the detachment of Co_3O_4 nanoparticles into the electrolyte. Luo *et al.* introduced flexible $Ti_3C_2T_x/V_2O_5$ films as supercapacitor electrodes using a vacuum-assisted filtration technique.[80] The addition of V_2O_5 nanofibers effectively mitigated MXene self-stacking and allowed precise control over film thickness, resulting in improved electrochemical performance. The $Ti_3C_2T_x/V_2O_5$ film achieved a capacitance of 319.1 F g^{-1} at 0.5 A g^{-1} (Fig. 5a) and maintained 70.4% of its capacitance after 5000 cycles at 3 A g^{-1} (Fig. 5b).

Two separate studies were carried out by Ambade *et al.*[81] and Peng *et al.*[82] on the synthesis and utilization of MXene–WO_3 composite for supercapacitor applications. In the study by Ambade *et al.*, Mono WO_3–Ti_3C_2 and Hexa WO_3–Ti_3C_2 hybrids were synthesized using a one-step hydrothermal method, with precise control over the phase of WO_3.[81] In the Mono WO_3–Ti_3C_2 hybrids, WO_3 nanorods filled the interlayer voids between the MXene sheets (Fig. 5c). In contrast, the Hexa WO_3–Ti_3C_2 hybrids featured WO_3 nanoparticles that were uniformly decorated over the MXene sheets (Fig. 5d). The electrochemical performance comparison reveals that the 2D synergetic hybrid architecture of Hexa WO_3–Ti_3C_2 nearly doubles the specific capacitance compared to Mono WO_3. The superior performance of Hexa WO_3–Ti_3C_2 compared to Mono WO_3–Ti_3C_2 and pristine WO_3, is attributed to its structural peculiarities,

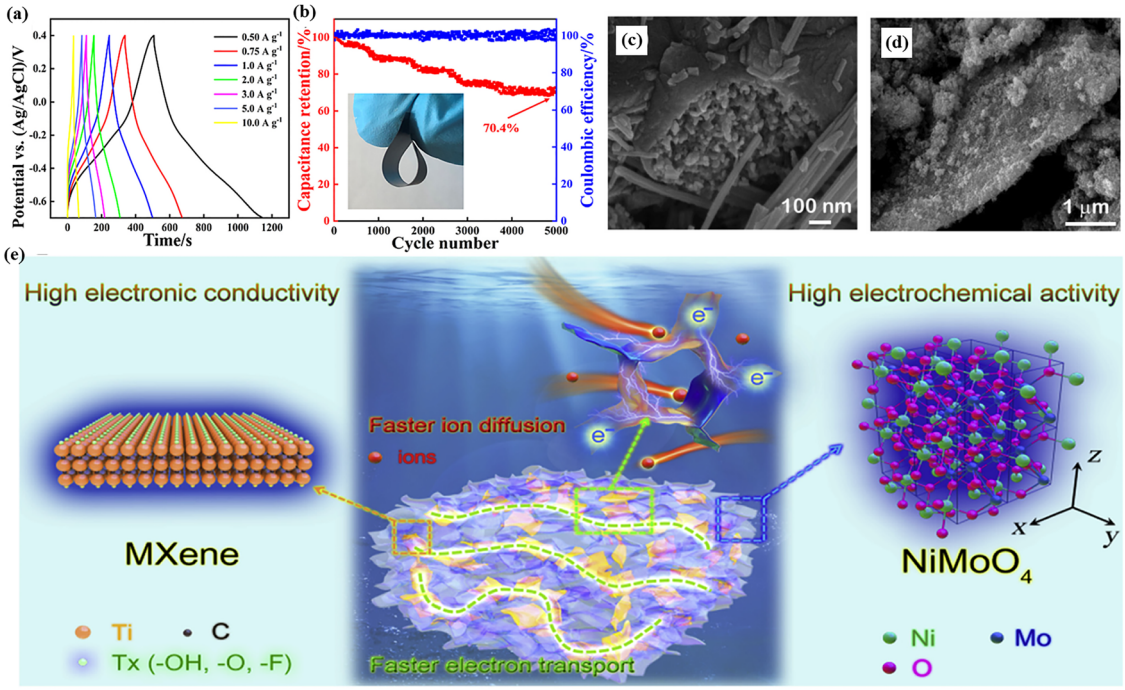

Fig. 5 (a) GCD curve of $Ti_3C_2T_x/V_2O_5$. Reproduced with permission from ref. 80 copyright 2023, Elsevier. (b) Stability test of $Ti_3C_2T_x/V_2O_5$. Reproduced with permission from ref. 80 copyright 2023, Elsevier. (c) SEM image of Mono WO_3–Ti_3C_2. Reproduced with permission from ref. 81 copyright 2018, John Wiley and Sons. (d) SEM image of Hexa WO_3–Ti_3C_2. Reproduced with permission from ref. 81 copyright 2018, John Wiley and Sons. (e) Schematic representation showing synergistic interaction between $NiMoO_4$ and $Ti_3C_2T_x$. Reproduced with permission from ref. 86 copyright 2019, Elsevier.

which provide more active sites for charge storage, and its increased specific surface area, facilitating efficient charge intercalation and deintercalation, thereby enhancing overall electrochemical performance. Meanwhile, in Peng's work, WO_3 nanorods/MXene composites were synthesized using an electrostatic self-assembly method, achieving a capacitance of 297 F g^{-1} at a current density of 1 A g^{-1} in 0.5 M H_2SO_4 electrolyte.[82]

3.1.7. MXene/binary TMO composites. Binary transition metal oxides are gaining attention for their battery-type behavior, multiple oxidation states, and higher electrical conductivity than single metal oxides. However, issues like agglomeration and low conductivity still limit their electrochemical performance.[83,84] MXene, known for its high conductivity, serves as a substrate for growing binary transition metal oxides, while binary transition metal oxides act as spacers. This synergy between MXene and binary transition metal oxides is expected to enhance electrochemical properties, with binary oxides offering superior crystal effects compared to single-metal oxides.[85] Wang *et al.* modified MXene with $NiMoO_4$, resulting in an interconnected porous structure that facilitates electrolyte ion diffusion during the electrochemical processes, thereby enhancing its capacity.[86] The synergistic effect between $NiMoO_4$ and $Ti_3C_2T_x$ (Fig. 5e) leads to a high specific capacity of 545.5 C g^{-1} at 0.5 A g^{-1}. Additionally, an ASC was fabricated by pairing the $NiMoO_4$/$Ti_3C_2T_x$ cathode with a rGO hydrogel anode, achieving an energy density of 33.76 Wh kg^{-1}.

Recently, Ni–Co bimetallic oxides have gained significant research interest as pseudocapacitive materials owing to their enhanced capacitance, improved charge transfer, and faster surface redox reaction kinetics. Song and his team combined Co_2NiO_4 bimetallic oxide with $Ti_3C_2T_x$ MXene through a hydrothermal synthesis method to develop advanced electrode materials for energy storage.[87] The integration leveraged the synergistic effects between Co_2NiO_4 and MXene, resulting in significantly enhanced specific capacitance and excellent long-term cycle stability. In another research, Co–Ni bimetallic oxides were deposited on $Ti_3C_2T_x$ MXene nanosheets using atomic layer deposition, a precise technique that ensures uniform integration and structural stability during redox processes.[88] The synergistic properties of CoO_x and NiO enhance pseudocapacitive performance, with CoO_x increasing oxidation potential and NiO enabling efficient electron transport. The dual-component CoO_x–NiO provides more active sites, while the high surface area of MXene sheets improves electrolyte interaction. Additionally, the hydrophilic functional groups and 2D structure of MXene facilitate effective ion intercalation, collectively leading to exceptional electrochemical performance of $x$$CoO_x$–NiO/$Ti_3C_2T_x$. Table 1 summarizes the synthesis strategies and C_{sp} of MXene/TMO composites for supercapacitor applications.

3.2. MXene/transition metal sulfides composites for supercapacitance studies

Transition metal sulfides have gained considerable attention in supercapacitor applications due to their exceptional electrochemical properties, including high theoretical capacitance, excellent conductivity, and abundant redox-active sites.[89] Materials such as MoS_2, NiS, and CoS exhibit pseudocapacitive behavior, where charge storage is facilitated by reversible faradaic reactions. However, challenges such as structural degradation during cycling, as well as complex synthesis processes, hinder their practical application. To overcome these issues, strategies like hybridization with carbon materials, heteroatom doping, and forming composites with MXenes have been explored.

3.2.1. MXene/molybdenum sulfide composites. MoS_2, a representative dichalcogenide material, has attracted considerable interest for its distinctive 2D characteristics. Notably, the 1T phase of MoS_2 offers superior conductivity, excellent hydrophilicity, increased interlayer spacing, and higher capacitance compared to the 2H phase.[90] Wang *et al.* developed a 1T-MoS_2/Ti_3C_2 MXene composite featuring a 3D interconnected network structure using a magneto-hydrothermal method.[91] This composite achieved a remarkable C_{sp} of 386.7 F g^{-1} at 1 A g^{-1} in 0.5 M H_2SO_4 (Fig. 6a), outperforming both 1T-MoS_2 and Ti_3C_2

Table 1 Synthesis strategies and C_{sp} of reported MXene/TMO composites for supercapacitor application

Electrode	Synthesis	Capacitance	Electrolyte	Challenge	Ref.
MXene/MnO_2	Hydrothermal	242 F g^{-1}, 1 A g^{-1}	0.5 M K_2SO_4	Agglomeration of MnO_2 particles on the MXene surface	48
Ti_3C_2/MnO_2	Electrostatic self-assembly	340 F g^{-1}, 1 A g^{-1}	1 M Na_2SO_4	Low cycling life	50
$Ti_3C_2T_x$/MnO_2	Vacuum-filtration	1025 F cm^{-3}, 0.2 mA cm^{-2}	PVA/LiCl	Aggregation of MnO_2 NWs on the MXene	51
MnO_2–Ti_3C_2 films	wet chemistry	602 F cm^{-3}, 2 mV s^{-1}	1 M Li_2SO_4	Low energy density	37
MnO_2@MXene/CNTF	Hydrothermal & coating	181.8 F g^{-1}, 1 A g^{-1}	1 M Na_2SO_4	High resistance for charge transfer	53
CC/MXene-MnO_2-CoNi-LDHs	Electrodeposition	922 F g^{-1}, 1 A g^{-1}	1 M KOH	Low surface area	54
Ti_3C_2/Mn_3O_4	Solvothermal method	128 mAh g^{-1}, 1 A g^{-1}	6 M KOH	Low-capacity retention	55
$Ti_3C_2T_x$/α-Fe_2O_3	Electrostatic self-assembly	405.4 F g^{-1}, 2 A g^{-1}	5 M LiCl	High contact resistance between the MXene and Fe_2O_3	59
Fe_3O_4/MXene/rGO	Chemical oxidation	42.8 F g^{-1}, 5 mV s^{-1}	5 M LiCl	Low capacitive retention	64
TiO_2/C-$Ti_3C_2T_x$-/NiO	Thermal annealing	92 mAh g^{-1}, 1 A g^{-1}	1 M KOH	Low capacitance retention	68
RuO_2@MXene-Ag	Chemical deposition	864.2 F cm^{-3}, 1 mV s^{-1}	PVA-KOH	—	78
$Ti_3C_2T_x$/V_2O_5	Vacuum-assisted filtration	319.1 F g^{-1}, 0.5 A g^{-1}	PVA/H_2SO_4	—	80
WO_3–Ti_3C_2	Electrostatic self-assembly	297 F g^{-1}, 1 A g^{-1}	0.5 M H_2SO_4	Low cyclic stability	82
$NiMoO_4$/$Ti_3C_2T_x$	Hydrothermal	545.5 C g^{-1}, 0.5 A g^{-1}	3 M KOH	—	86
Co_2NiO_4/$Ti_3C_2T_x$	Hydrothermal	719.5 F g^{-1}, 0.5 A g^{-1}	3 M KOH	—	87
xCoO_x-NiO/$Ti_3C_2T_x$	Atomic layer de- position	1960 F g^{-1}, 1 A g^{-1}	6 M KOH	—	88

MXene individually. The enhanced capacitance is credited to the synergistic interactions within the heterostructure, which promote efficient H^+ storage in the interconnected spaces between 1T-MoS_2 and Ti_3C_2 MXene. Meanwhile, Chandran *et al.* confined MoS_2 within MXene layers using an *in situ* wet impregnation method.[92] This approach filled the MXene stacks with MoS_2, resulting in a synergistic effect that provided more active sites for electrochemical reactions, reduced internal resistance, and enhanced ion transfer and pseudocapacitive behavior. The MoS_2/MXene composite exhibited a higher surface area of 67.30 $m^2\ g^{-1}$ and a pore volume of 0.077 $cm^3\ g^{-1}$, attributed to the confinement of MoS_2. This structural enhancement improved electrode–electrolyte interaction and boosted electrochemical performance. The composite displayed a quasi-rectangular CV response, which is a characteristic of pseudocapacitance, and achieved a maximum specific capacitance of 342 F g^{-1} at 0.4 A g^{-1} over a voltage range of −1.5 V to 1.5 V. Notably, it retained over 99% of its discharge capacity even after 10 000 cycles.

3.2.2. MXene/nickel sulfide composites. Among transition metal sulfides (TMS), Ni_3S_2 is notable for its high theoretical capacitance, excellent rate performance, low cost, and natural abundance.[93,94] Compositing has proven to be an effective strategy for enhancing its electrochemical performance. Zhao and his team pioneered the synthesis of a Ni_3S_2/d-Ti_3C_2 heterostructure for supercapacitor applications.[95] Fig. 6b shows that Ni_3S_2/d-Ti_3C_2/NF electrode delivered an exceptional C_{sp} of 2204 F g^{-1} at 1 A g^{-1}. An ASC, using this electrode as the positive electrode, activated carbon on Ni foam as the negative electrode, and KOH as the electrolyte, achieved an energy density of 23.6 Wh kg^{-1} and a power density of 4004.4 W kg^{-1}. The strong interaction among d-Ti_3C_2, Ni_3S_2, and Ni foam enhances charge transfer efficiency, leading to outstanding capacitance and rate performance. In a similar study, LuO *et al.* have synthesized Ni–S/d-Ti_3C_2 through a solvothermal approach, and the optimized Ni–S/1d-Ti_3C_2 nanohybrid achieves a high specific capacity of 840.4 C g^{-1} at 1 A g^{-1}, with 64.3% retention at 30 A g^{-1} and excellent cycling stability.[96] An asymmetric supercapacitor using Ni–S/1d-Ti_3C_2 as the positive electrode and d-Ti_3C_2 film as the negative electrode delivers an energy density of 20.0 Wh kg^{-1} at 0.5 kW kg^{-1} with reliable cycling stability.

3.2.3. Other MXene/TMS composites. Beyond Mo and Ni sulfides, CoS_2 is an excellent choice for supercapacitor electrode materials due to its low electronegativity, high electrical conductivity, substantial specific capacity, and abundant electrochemical redox sites.[97] However, when used alone, CoS_2 undergoes significant volume changes during redox processes, leading to reduced cycle stability and rate performance, which limits its practical application.[98] A promising approach to address this issue is combining CoS_2 with MXene to form a composite, enhancing its cycling stability and overall performance. Liu *et al.* synthesized a $Ti_3C_2T_x/CoS_2$ composite *via* a simple hydrothermal method and achieved a C_{sp} of 1320 F g^{-1} at 1 A g^{-1} and retained 78.94% of its capacitance after 3000 cycles.[98] When paired with rGO in an ASC, it demonstrated a high energy density of 28.8 Wh kg^{-1} at a power density of 800 W kg^{-1} and 98% cycling retention after 5000 cycles.

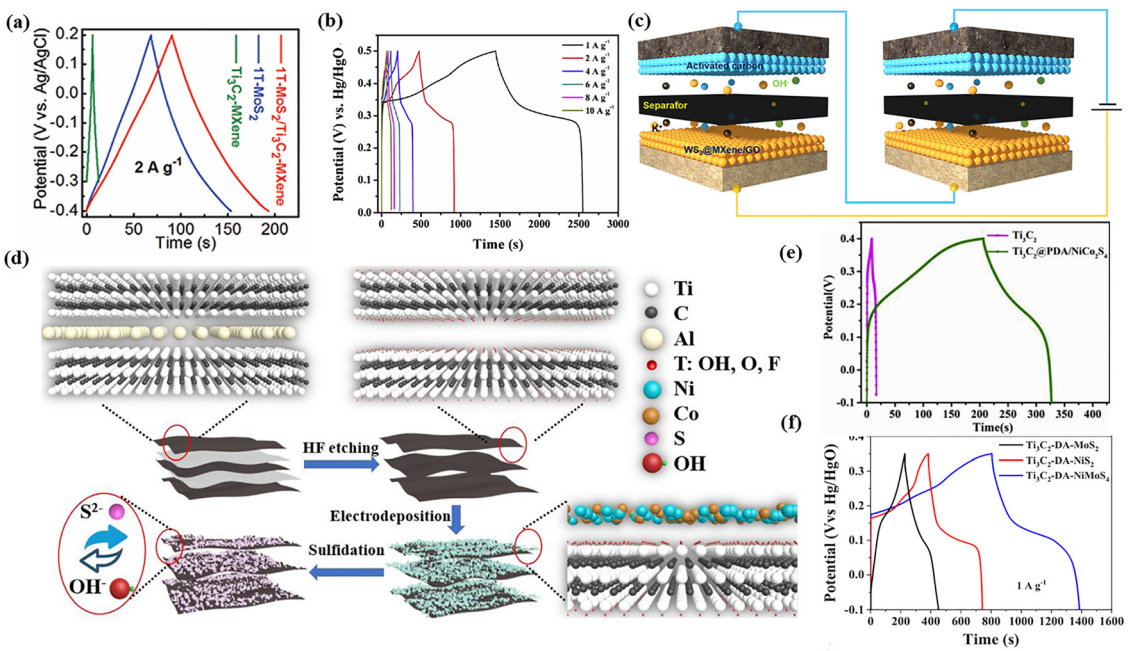

Fig. 6 (a) GCD curve of 1T-MoS_2, Ti_3C_2, and 1T-MoS_2/Ti_3C_2. Reproduced with permission from ref. 90 copyright 2020, MDPI. (b) GCD curve of Ni_3S_2/d-Ti_3C_2/NF. Reproduced with permission from ref. 95 copyright 2020, Elsevier. (c) schematic representation of WS_2@MXene/GO asymmetric device. Reproduced with permission from ref. 100 copyright 2023, Elsevier. (d) Fabrication of MXene-$NiCo_2S_4$. Reproduced with permission from ref. 103 copyright 2020, Elsevier. (e) GCD curve of Ti_3C_2 and Ti_3C_2@PDA/$NiCo_2S_4$. Reproduced with permission from ref. 106 copyright 2019, Elsevier. (f) GCD curve of Ti_3C_2-DA-MoS_2, Ti_3C_2-DA-NiS_2, and Ti_3C_2-DA-$NiMoS_4$. Reproduced with permission from ref. 107 copyright 2022, Elsevier.

Limited research has focused on WS_2-integrated MXenes for energy storage applications. Vyskočil and colleagues investigated the enhancement of charge storage capacitance by incorporating 1T-phase WS_2 nanospacers into the MXene matrix using a simple sonication-assisted method.[99] The optimal 10%:90% ratio of 1T-phase WS_2 to Ti_3C_2 resulted in a C_{sp} of 157.0 F g^{-1}, nearly double that of pure Ti_3C_2 MXene, demonstrating a significant improvement in charge storage performance. In a study conducted by Hussain and his co-workers, porous WS_2 nanosheets-interconnected MXene/GO composites were synthesized using the hydrothermal method and utilized as electrode materials for supercapacitors.[100] The composite achieved a C_{sp} of 1111 F g^{-1} at a current density of 2 A g^{-1}, while the asymmetric device (Fig. 6c), demonstrated a high specific energy of approximately 114 Wh kg^{-1} and exceptional cycling stability.

3.2.4. MXene/binary TMS composites. Recent research shows that bimetallic sulfides offer a combination of higher capacitance, improved stability, enhanced conductivity, and superior performance compared to monometallic sulfides, making them a more promising option for supercapacitors. In particular, $NiCo_2S_4$, a novel bimetallic sulfide, has been extensively studied due to its excellent electrical conductivity, low charge transfer resistance, and promising theoretical specific capacity.[101] However, similar to other pseudocapacitive electrode materials, $NiCo_2S_4$ experiences structural expansion and contraction during cycling, resulting in poor cycling stability, with typically 50–70% capacity retention.[102] Li *et al.* developed a novel 3D MXene-$NiCo_2S_4$ nanostructure as a binder-free electrode for supercapacitors, addressing the limitations of MXene's low capacitance and the weak cycling stability and conductivity of transition metal sulfides.[103] The process began by directly coating MXene clay onto nickel foam without a binder, which reduced internal resistance and enhanced charge transport. $NiCo_2S_4$ precursor was then electrodeposited onto the MXene nanosheets, followed by the addition of sodium sulfide nonahydrate and sulfuration through hydrothermal anion-exchange reactions (Fig. 6d), resulting in a composite with enhanced surface area and a specific capacity of 596.69 C g^{-1} at 1 A g^{-1}. The MXene-$NiCo_2S_4$@NF composite retained 80.4% of its initial capacitance after 3000 cycles, demonstrating excellent cycling stability compared to pure MXene. The fabricated asymmetric solid-state supercapacitor achieved an energy density of 27.24 Wh kg^{-1} at a power density of 0.48 kW kg^{-1}. This composite outperformed both pure MXene and pure $NiCo_2S_4$ due to the synergistic effects of MXene's high surface area and improved conductivity, as well as $NiCo_2S_4$'s enhanced specific capacity driven by rapid redox reactions involving Ni^{2+}/Ni^{3+} and $Co^{2+}/Co^{3+}/Co^{4+}$ during charge–discharge cycles.

In a similar study, Wu *et al.* synthesized P-Ti_3C_2@ $NiCo_2S_4$ nanocomposites by hybridizing 1D $NiCo_2S_4$ hollow nanotubes with 2D P-Ti_3C_2 MXene using a hydrothermal method.[104] Compared to previous studies, the P-Ti_3C_2@ $NiCo_2S_4$ composite exhibited significantly enhanced C_{sp} of 1927 F g^{-1} at 2 mV s^{-1}, superior cycling stability, low internal resistance, and excellent rate performance. These improvements are attributed to the unique hollow tubular structure of $NiCo_2S_4$, which increases the specific surface area and facilitates ion transport. Additionally, the Ti_3C_2 conductive matrix stabilizes the structure by mitigating volume changes in $NiCo_2S_4$ during prolonged cycles, preventing structural collapse. Meanwhile, He *et al.* developed $Ni_{1.5}Co_{1.5}S_4$@Ti_3C_2 hybrid materials by *in situ* growth of $Ni_{1.5}Co_{1.5}S_4$ nanoparticles on Ti_3C_2 MXene nanoflakes through a one-step hydrothermal method.[105] By optimizing the composition and achieving maximum synergistic effects, the electrode exhibited a high C_{sp} of 166.7 mAh g^{-1}, with a 73.9% retention rate after a 20-fold increase in current density. Furthermore, the assembled ASC delivered an energy density of 49.8 Wh kg^{-1} at 800 W kg^{-1} and maintained 90% capacitance retention over 8000 cycles, demonstrating excellent performance and durability. Meanwhile, Wu *et al.* developed Ti_3C_2@PDA/$NiCo_2S_4$ composites as high-performance supercapacitor electrodes, and claimed that the polydopamine (PDA) coating on Ti_3C_2 surface prevents its structural collapse and oxidation during hydrothermal synthesis.[106] Additionally, the confined synthesis of smaller $NiCo_2S_4$ particles between Ti_3C_2 layers prevents restacking, increases accessible surface areas, and enhances charge transfer and ion diffusion. As given in Fig. 6e, the composite achieved a specific capacitance of 495 F g^{-1} at 2 mV s^{-1}, a tenfold increase compared to pristine Ti_3C_2, with exceptional cycling stability, retaining 81.16% of capacitance after 3000 cycles. Xu *et al.* prepared ultrathin Ti_3C_2 MXenes incorporated with a high density of $NiMoS_4$ nanoparticles, utilizing dopamine, and it demonstrated an impressive C_{sp} of 1288 F g^{-1} at 1 Ag^{-1} (Fig. 6f).[107]

3.3. MXene/transition metal selenides composites for supercapacitance studies

Transition metal diselenides share similarities with transition metal sulfides, as selenium and sulfur belong to the same group due to selenium's higher density and electrical conductivity, transition metal selenides may offer superior volume energy density and rate capability compared to transition metal sulfides.[108]

Recently, there has been growing interest in transition metal selenides as electrode materials for electrochemical energy storage applications. Jiang *et al.* were the first to introduce the combination of MXene and transition metal selenides for energy storage applications.[109] The electrochemical performance of Ti_3C_2/$NiSe_2$ is compared with pristine $NiSe_2$. Ti_3C_2/$NiSe_2$ exhibits a high C_{sp} value of 531.2 F g^{-1}, and a lower R_{ct} of 95.4 mΩ, suggesting the formation of an efficient conductive network. In a similar study by Hussain *et al.*, $MoSe_2$/MXene was utilized as an effective electrode for supercapacitors, delivering a C_{sp} of 350 F g^{-1} and achieving 93% capacitance retention over 5000 cycles.[110] In recent times, MXene/WSe_2 hybrids have been prepared hydrothermally, and the fabricated symmetric supercapacitor delivers C_{sp} of 246 F g^{-1} at 2 A g^{-1}.[111]

One of the major bottlenecks in preparing MXene/TMO and MXene/TMC composites is the rapid oxidation of MXenes, especially in aqueous media in the presence of transition metal ions. Wang *et al.* demonstrated that Co^{2+} accelerates $Ti_3C_2T_x$

oxidation by enhancing water reactivity, but this drawback was mitigated by introducing *N*,*N*-dimethylformamide (DMF), which preferentially coordinates with Co^{2+} and reduces water activity, thereby stabilizing MXene and enabling the successful synthesis of $CoO/Ti_3C_2T_x$ composites.[112] Another study elucidated that Fe^{3+} promotes MXene oxidation by inducing electron loss and generating hydroxyl radicals, but a two-in-one strategy using $ZnNa_2EDTA$ effectively suppressed this process by defect filling and electron donation, significantly enhancing MXene's oxidation tolerance even in the presence of Cu^{2+}.[113] These two works highlight solvent and additive engineering as powerful approaches to prevent oxidative degradation during composite formation. In contrast, Xu *et al.* approached the oxidation issue from a different angle by employing a solvent-free ultrasound-assisted ball milling strategy to fabricate SnS_2@C/MXene composites.[114] This method bypassed the aqueous oxidation pathway entirely, while simultaneously improving interlayer spacing, electronic conductivity, and structural stability, yielding outstanding lithium storage performance. Taken together, these studies demonstrate that oxidation challenges in MXene-based composite synthesis can be addressed either by chemically suppressing oxidative pathways or by adopting alternative, non-aqueous synthesis routes, both of which are crucial for realizing the full potential of MXene/TMO and MXene/TMC systems in energy storage applications.

This section offers an in-depth overview of MXene composites with transition metal oxides and chalcogenides, emphasizing their synergistic interactions and impact on energy storage. Ongoing research highlights the significant progress of MXene hybrids in energy storage applications.

4. MXene-based composites for overall water splitting

MXenes have emerged as transformative materials in electrocatalysis, particularly for water splitting applications. When combined with transition metal oxides and chalcogenides, these composites pair the stability and catalytic activity of the oxides and chalcogenides with the excellent electron transfer abilities of MXenes. This powerful synergy boosts catalytic efficiency, lowers energy barriers, and drives the development of cost-effective and sustainable hydrogen production solutions.

4.1. MXene/transition metal oxide composites for overall water splitting

Oxides of transition metals like Co, Mn, Mo, V, Ni, Fe, and Cu have been widely utilized in water-splitting applications. However, many transition metal oxides suffer from low electronic conductivity, which hampers efficient electron transport.[89] Integrating MXenes with transition metal oxides promotes rapid charge transport and provides abundant active sites for hydrogen adsorption.

4.1.1. MXene/cobalt oxide composites. Cobalt oxide, among various transition metal oxides, has been widely studied as an efficient catalyst for water splitting. However, cobalt oxide alone often exhibits low catalytic activity due to its limited intrinsic electrical conductivity and tendency to self-aggregate.[115] To overcome these drawbacks, coupling cobalt-based composites with highly conductive carbon materials, such as MXenes, has proven effective in enhancing charge transport, minimizing aggregation, and boosting catalytic performance.

In this context, Lu *et al.* synthesized 0D Co_3O_4/2D Ti_3C_2 MXene heterojunctions using *in situ* electrostatic assembly followed by a solvothermal technique. This approach ensured uniform anchoring of Co_3O_4 nanoparticles onto Ti_3C_2 MXene nanosheets, driven by strong interfacial interactions and effective electronic coupling.[116] The Co_3O_4/Ti_3C_2 MXene shows an overpotential of 300 mV at 10 mA cm^{-2} in 1 M KOH, surpassing the performance of both Ti_3C_2 MXene and Co_3O_4. It also achieves a lower Tafel slope (118 mV dec^{-1}) compared to Co_3O_4 (153 mV dec^{-1}) and MXene (442 mV dec^{-1}). This exceptional catalytic performance and stability are attributed to strong interfacial electrostatic interactions, which enhance electron transport, increase electrical conductivity, provide abundant active sites, and reduce charge transfer pathways, collectively boosting electrocatalytic efficiency. However, the limitation of this study is that the catalyst performs poorly in OER, preventing it from functioning as a bifunctional catalyst. To overcome the previous limitations, Sunny *et al.* developed a $Ti_3C_2T_x/Co_3O_4$ nanocomposite using sonication.[117] Their findings demonstrated that the 1 : 2 ration of $Ti_3C_2T_x/Co_3O_4$ outperformed the individual components, achieving the lowest overpotential of 270 mV at 50 mA cm^{-2} and the smallest Tafel slope of 85 mV dec^{-1} for OER. Furthermore, $Ti_3C_2T_x/Co_3O_4$ (2 : 1) exhibited an overpotential of 235 mV at 50 mA cm^{-2} and the lowest Tafel slope of 97 mV dec^{-1} for HER. The enhanced oxygen-functional groups in $Ti_3C_2T_x$ offer adsorption sites for hydrogen, accelerating HER, while cobalt oxide promotes charge transfer to the electronegative MXene, stabilizing the catalyst. Meanwhile, for OER, the cobalt centres acted as active sites while MXene served as a support matrix to prevent Co_3O_4 nanoparticle aggregation. When paired, $Ti_3C_2T_x/Co_3O_4$ (2 : 1) as the cathode and $Ti_3C_2T_x/Co_3O_4$ (1 : 2) as the anode, the total electrolysis voltage required to achieve a current density of 10 mA cm^{-2} was 1.73 V, while showing satisfactory stability.

In another study by Guo *et al.*, a bifunctional catalyst for overall water splitting was developed by combining a Co-based dual-active heterojunction, Co–CoO, with MXene layers through *in situ* electrostatic assembly, followed by reduction.[118] MXene prevented the aggregation of Co–CoO and enhanced conductivity, boosting both activity and stability. The Co–CoO/Ti_3C_2-MXene catalyst exhibited a low onset potential of 8 mV and a Tafel slope of 47 mV dec^{-1} for HER (Fig. 7a and b), and an onset potential of 196 mV with a Tafel slope of 47 mV dec^{-1} for OER (Fig. 7c and d). The cell demonstrated a low voltage of ~1.55 V at 10 mA cm^{-2}, high faradaic efficiency, and remarkable stability, making it suitable for overall water splitting. DFT calculations were conducted to clarify the catalytic mechanism of Co–CoO/Ti_3C_2-MXene. The density of states (DOS) revealed enhanced electronic coupling in Co–CoO/Ti_3C_2-MXene, leading to superior

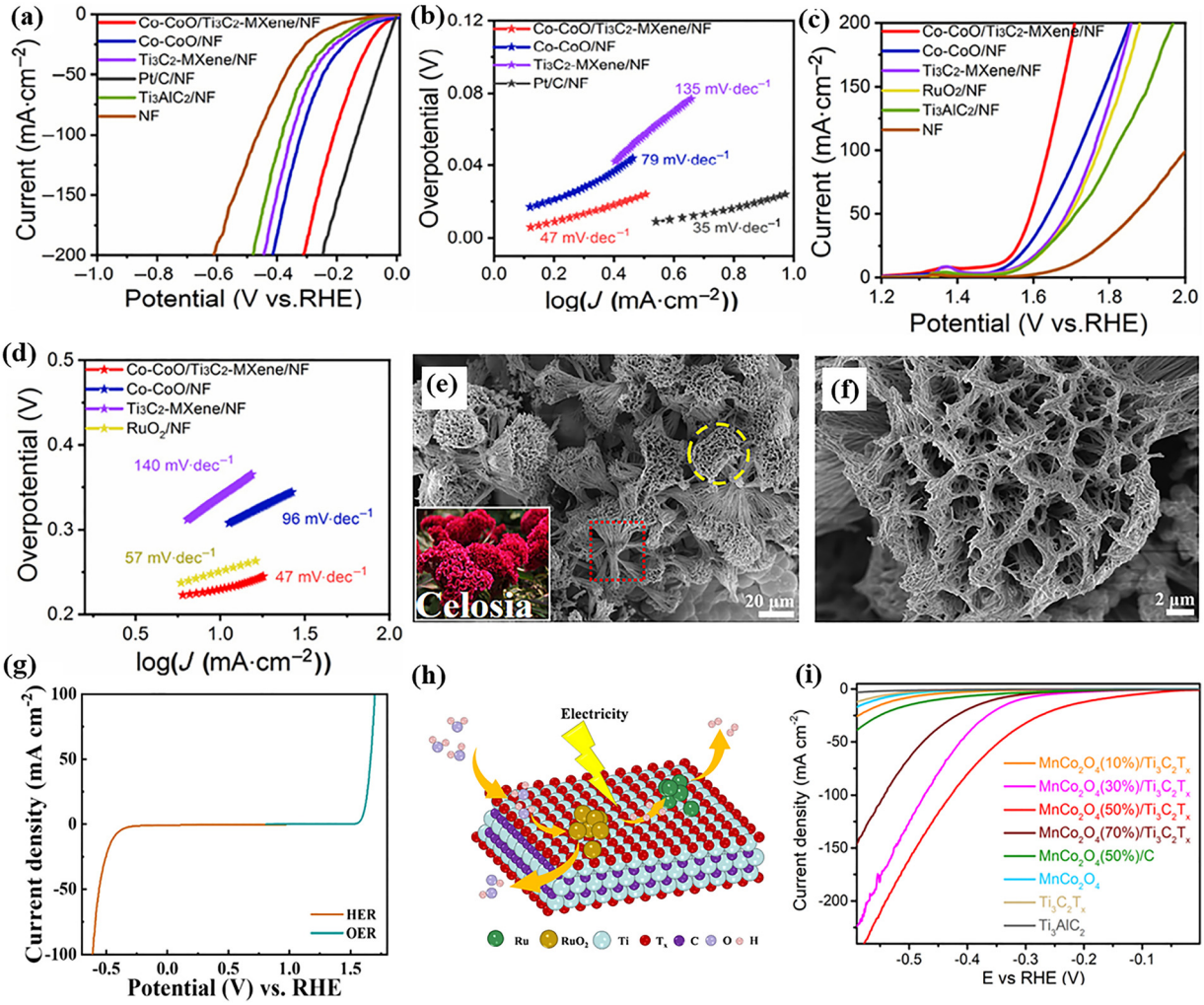

Fig. 7 Overall water splitting analysis of of Co–CoO/Ti_3C_2/NF, Ti_3C_2/NF, and Co–CoO/NF. Reproduced with permission from ref. 118 copyright 2021, Springer Nature. (a) LSV curves for HER (b) Tafel plots for HER (c) LSV curves for OER (d) Tafel plots for OER (e and f) SEM images of P–MoO_3 FCL MXene/NF. Reproduced with permission from ref. 121 copyright 2022, Elsevier. (g) LSV curve of Na-MnO_{2-x} Reproduced with permission from ref. 123 copyright 2024, Elsevier. (h) Diagrammatic representation working mechanism of Ru–RuO_2/MXene@CC catalyst. Reproduced with permission from ref. 125 copyright 2023, Elsevier. (i) LSV curves for $MnCo_2O_4/Ti_3C_2T_x$. Reproduced with permission from ref. 133 copyright 2022, Elsevier.

conductivity compared to individual components. The calculated adsorption free energy (ΔG_{H^*}) confirmed that metallic Co sites (0.232 eV) act as the primary active centers for HER, while Co^{2+} sites dominate OER activity with the lowest rate-determining step energy (1.325 eV). These results demonstrate that the synergistic interaction between Co–CoO and Ti_3C_2-MXene optimizes electronic structure, enhances conductivity, and reduces reaction barriers, thereby boosting both HER and OER performance.

4.1.2. MXene/molybdenum oxide composites. MoO_3 is recognized as a promising material for electrocatalytic applications due to its favourable crystal structure, versatile oxidation states, and high surface area. However, its low electrical conductivity and suboptimal adsorption energy of reaction intermediates limited its broader application.[119] The introduction of oxygen vacancies and the integration of MoO_3 with conductive support were found to significantly enhance its electronic properties.[120] In another study, Li and colleagues developed a 3D porous "celosia-like" framework composed of FeCo-layered double hydroxide and phosphorus-doped molybdenum oxide grown *in situ* on MXene-modified nickel foam.[121] The Celosia-like structure of the composite, as shown in Fig. 7e and f, features small spikes that serve as highly efficient conductive bridges, accelerating charge transfer during the catalytic process and enhancing electrochemical performance. DFT calculations revealed that tuning the electron distribution at the P-MoO_3 and FeCo-LDH interface optimized electron transfer rates and lowered the adsorption energy of reaction intermediates like H*, OH*, and OOH*. Benefiting from the synergistic chemical and electronic interactions within the heterogeneous structure, the catalyst demonstrated exceptional performance for OER and HER, achieving low overpotentials of 179 mV and 118 mV at 10 mA cm^{-2}, respectively, and a faradaic efficiency of 96%. Notably, the catalyst required only 1.53 V to drive a current density of 10 mA cm^{-2} in a two-electrode setup.

Iffat *et al.* employed a hydrothermal method to synthesize MoO_3 nanobelts, which were uniformly anchored onto Ti_3C_2 MXene sheets, resulting in the formation of Ti_3C_2@MoO_3 nanobelts.[122] In the Ti_3C_2@MoO_3 nanocomposite, Ti_3C_2 acted as a conductive matrix, enabling efficient electron transfer, while MoO_3 provided long-term stability and prevented the restacking of Ti_3C_2 nanosheets. This synergy significantly enhanced HER and OER performance, achieving low overpotentials of 91 mV and 190 mV, respectively, at a current density of 10 mA cm^{-2}, with stability maintained for 50 h. The combined presence of Ti and Mo improved electrocatalytic activity through efficient orbital overlap and electronic density fluctuations, promoting better interaction with reaction intermediates.

4.1.3. Other MXene/TMO composites. Apart from cobalt and molybdenum oxides, other transition metal oxides, such as manganese, vanadium, and ruthenium, have also been combined with Ti_3C_2 MXene and investigated for water splitting applications. Vetrikarasan and his team synthesized oxygen vacancy-enriched Na-MnO_{2-x} using an electrodeposition method.[123] The enriched oxygen vacancies significantly enhanced the electrode's conductivity and reaction kinetics, demonstrating efficient HER and OER performance with overpotentials of 439.7 mV and 381.2 mV at 10 mA cm^{-2} (Fig. 7g). Iffat *et al.* synthesized d-Ti_3C_2/V_2O_5 nanohybrid using a hydrothermal method, and it demonstrated outstanding electrocatalytic performance, achieving low overpotentials of 90 mV for HER and 240 mV for OER at 10 mA cm^{-2}, with Tafel slopes of 49 mV dec^{-1} and 52 mV dec^{-1} in 1.0 M KOH.[124] It delivered exceptional overall water-splitting efficiency, requiring a cell voltage of just 1.45 V at 10 mA cm^{-2}, and maintained excellent stability with minimal degradation at 0.6 V over 24 h. In another study, Shi *et al.* presented a method to optimize the Ru–RuO_2 heterointerface proportion in Ru–RuO_2/MXene@CC catalyst by tuning the Ru content.[125] Adjusting the Ru loading to 3 wt% improved the water contact angle from 57.4° to 25.5°, enhancing hydrophilicity. At this optimal loading, the catalyst demonstrated superior HER performance, achieving a low overpotential of 43 mV at 10 mA cm^{-2}, a Tafel slope of 52.1 mV dec^{-1}, and a mass activity of 1751.11 mA mg^{-1}. It also showed remarkable stability, maintaining performance over 10 h in alkaline conditions. As illustrated in Fig. 7h, the hydrophilic nature of MXene enables close interaction with water molecules, while Ru effectively dissociates these molecules, facilitating the Volmer step in the HER process. Concurrently, RuO_2 enhances the decomposition of H*, driving the Heyrovsky step. The combined action of Ru, RuO_2, and MXene improves charge transfer within the catalyst, significantly boosting HER efficiency. Additionally, the carbon cloth (CC) substrate provides excellent stability and conductivity, further supporting catalyst durability and efficient electron transport. These attributes make the Ru–RuO_2/MXene@CC catalyst a highly stable and efficient catalyst for hydrogen generation.

Recently, spinel metal oxides with the general formula AB_2O_4 have garnered significant attention across various electrocatalytic applications, especially in energy generation and storage.[126,127] Among these, the inverse spinel structure $NiFe_2O_4$ is particularly advantageous for electrocatalysis due to its diverse redox states, excellent electrochemical stability, high abundance, low toxicity, and affordability.[128] Shinde *et al.* combined the distinctive properties of 2D Ti_3C_2 MXene with spinel $NiFe_2O_4$ to develop a composite material with significant potential for electrocatalytic water splitting.[129] The $NiFe_2O_4$/Ti_3C_2 composite synthesized through one-pot hydrothermal method showed excellent electrocatalytic performance with low overpotentials of 266 mV for OER and 173 mV for HER at 10 mA cm^{-2} in 0.5 M KOH. Its superior activity is attributed to the nanoparticle-sheet interface, synergistic effects, and the high conductivity of Ti_3C_2 MXene, which enhances active site availability and efficiency. DFT calculations were conducted to evaluate the overpotentials of the $NiFe_2O_4$/Ti_3C_2 composite for both OER and HER, with the outcomes compared to experimental data. The theoretical overpotentials were calculated to be 337.3 mV for OER and 238.2 mV for HER, values that are in close agreement with the experimentally measured results and follow the same trend. This strong correlation confirms the consistency between theoretical predictions and experimental observations, thereby validating the reliability of the computational model in accurately describing the catalytic behavior of the $NiFe_2O_4$/Ti_3C_2 composite.

Subsequent studies have shown that $CoNiFe_2O_4$ offers significant advantages over $NiFe_2O_4$ due to its superior magnetic anisotropy, minimal electrical resistivity, higher thermal stability, and superparamagnetic properties. In Ni–Co bimetallic material, cobalt facilitates partial electron transfer to neighbouring nickel sites, increasing proton adsorption and enhancing charge transfer, which accelerates HER activity. Combining the properties of 2D MXene with $CoNiFe_2O_4$ presents a promising strategy for developing high-performance electrocatalysts for water splitting, surpassing the performance of pristine $NiFe_2O_4$ and MXene. In this context, Rasheed *et al.* fabricated a $CoNiFe_2O_4$/MXene composite using a layer-by-layer assembly method.[130] The resulting catalyst exhibited excellent overpotentials of 149 mV and 17 mV at 10 mA cm^{-2} for OER and HER, respectively, with Tafel slopes of 36 mV dec^{-1} (HER) and 45 mV dec^{-1} (OER). Furthermore, it demonstrated remarkable electrochemical stability, maintaining the performance for up to 100 h.

Ruthenium-based spinel metal oxides are a cost-effective alternative to Pt-based catalysts for HER, with strong hydrogen bonding efficiency and potential for overall water splitting.[131] Parv *et al.* developed a $RuCo_2O_4$@$Ti_3C_2T_x$@NF nanohybrid using electrodeposition, achieving low overpotentials for both HER (68 mV) and OER (170 mV).[131] For overall water splitting, it demonstrated a cell voltage of 1.62 V and enhanced durability over 24 h at 10 mA cm^{-2}. DFT studies confirmed strong $RuCo_2O_4$-Ti_3C_2 binding, charge redistribution at the interface, and optimized d-orbital energy levels, improving intermediate binding and electron transfer efficiency. These properties make it a robust and efficient catalyst for water splitting. In another study based on spinel metal oxides, Ghorbanzadeh and his team synthesized a hybrid catalyst by integrating $CuCo_2O_4$ with

$Ti_3C_2T_x$ MXene through a solvothermal method, followed by post-annealing.[132] The resulting ultrathin structure, with a large surface area, significantly increased the number of electrochemically active sites, enhancing electrocatalytic performance. Experimental results demonstrated that the $CuCo_2O_4$/$Ti_3C_2T_x$ hybrid on nickel foam exhibited superior OER activity compared to pristine $Ti_3C_2T_x$ with a low overpotential of 1.67 V at 100 mA cm^{-2}, a small Tafel slope of 49 mV dec^{-1}, and excellent long-term durability. In a related study, nanosized spinel $MnCo_2O_4$ was effectively integrated with ultrathin $Ti_3C_2T_x$ MXene nanosheets using a simple, cost-efficient method.[133] Traditional bulk $MnCo_2O_4$ often traps numerous catalytically active sites within its structure, and its inherent semiconducting nature typically leads to sluggish charge transfer kinetics, limiting its large-scale application in electrocatalysis. However, the combination of $MnCo_2O_4$ with $Ti_3C_2T_x$ nanosheets introduces several advantageous structural features and strong synergistic effects, including high surface areas, close 0D/2D interfacial contact, unveiling of active sites, optimized electronic properties, and enhanced electron conductivity. As shown in Fig. 7i, the $MnCo_2O_4$/$Ti_3C_2T_x$ electrocatalyst exhibited remarkable HER performance with a low onset potential of 51 mV, and better long-term stability than pristine $MnCo_2O_4$ and $Ti_3C_2T_x$ catalysts.

Recent progress in electrocatalyst development has highlighted the potential of high-entropy materials (HEMs) when combined with MXenes for advancing OER technologies. Park *et al.* demonstrated this concept by integrating a high-entropy oxide (HEO), composed of V, Mn, Co, Fe, and Ni oxides, with $Ti_3C_2T_x$ MXene through microwave treatment followed by low-temperature calcination.[134] The resulting HEO/$Ti_3C_2T_x$ hybrid delivered an overpotential of 331 mV at 10 mA cm^{-2} in 1 M KOH, surpassing the benchmark IrO_2 catalyst. The superior activity was attributed to the strong interfacial coupling between HEO and MXene, which facilitated electronic structure modulation, increased the density of accessible active sites, and accelerated charge transfer owing to the excellent conductivity of $Ti_3C_2T_x$. This work provided compelling evidence for the effectiveness of entropy-stabilized multi-component oxides when anchored on conductive MXenes.

Expanding on these findings, Li *et al.* developed MOF-derived high-entropy $(FeCoNiCuMn)_2O_3$ nanoparticles supported on $Ti_3C_2T_x$ MXene using a solvothermal method, yielding a MXene/HEO composite.[135] This catalyst exhibited outstanding OER activity not only in alkaline electrolytes but also in simulated seawater, maintaining stable performance for 300 h without noticeable degradation. The exceptional durability and activity were attributed to intrinsic entropy stabilization, multi-metallic synergy, and strong coupling with MXene. Theoretical calculations revealed that the OER proceeded through an ''Absorption–Migration'' mechanism (AMM), which enhanced activity compared to the conventional AEM pathway. This study introduced a valuable approach to designing chloride-resistant electrocatalysts for practical seawater electrolysis.

In another complementary work, Li *et al.* synthesized an amorphous high-entropy borate ($FeCoNiMnBO_x$) integrated with Ti_3C_2 MXene *via* a low-temperature liquid-phase reduction strategy.[136] The $FeCoNiMnBO_x$/MXene composite achieved an impressively low overpotential of 268 mV at 10 mA cm^{-2} and a Tafel slope of 39.8 mV dec^{-1}, outperforming both pristine $FeCoNiMnBO_x$ and RuO_2. The amorphous structure of $FeCoNiMnBO_x$ exposed abundant active sites, while the lamellar MXene effectively inhibited particle aggregation and improved catalytic site accessibility. Furthermore, strong interfacial bonding induced charge redistribution and promoted rapid electron transfer, thereby enhancing conductivity and facilitating the oxidation of transition–metal ions within the borate phase.

Collectively, these studies highlight the effectiveness of coupling HEMs with MXenes as a versatile strategy for designing next-generation OER electrocatalysts. The crystalline HEO/MXene hybrid capitalized on electronic modulation, the MOF-derived MHEO/MXene offered long-term stability and anti-chloride resistance, while the amorphous HEB/MXene maximized active site exposure through structural disorder. Despite these different structural approaches, a unifying theme across all systems was the pivotal role of interfacial coupling in enabling efficient charge transfer, enhancing stability, and mitigating catalyst deactivation. Together, these findings underscore the promise of MXene/HEM composites as robust, durable, and cost-effective electrocatalysts, paving the way toward practical and sustainable energy conversion technologies.

4.2. MXene/transition metal sulfides composites for overall water splitting

4.2.1. MXene/molybdenum sulfide composites. Apart from this, MXene-transition metal sulfide composites have been extensively explored for their synergy in energy related applications. Attanayake *et al.*[137] and Huang *et al.*[138] independently explored the integration of vertically aligned MoS_2 nanoparticles on Ti_3C_2 MXene layers. In Attanayake's study, a microwave-assisted colloidal synthesis method was employed to produce the $MoS_2 \perp Ti_3C_2$ composite, which expanded the interlayer spacing of MXene to 9.4 Å, exposing more active sites.[137] This composite demonstrated a low overpotential of 95 mV and a Tafel slope of 40 mV dec^{-1} for HER (Fig. 8a and b). Conversely, Huang's work utilized a hydrothermal method for the *in situ* growth of MoS_2 on planar Ti_3C_2 nanosheets.[138] The resulting layered structure, with vertically aligned MoS_2 on Ti_3C_2, created porous networks and open channels that enhanced reactant adsorption and diffusion. This design achieved an overpotential of 280 mV and a Tafel slope of 68 mV dec^{-1} for HER (Fig. 8c and d).

Another study reported the fabrication of hierarchical MoS_2/Ti_3C_2-MXene@C nanohybrids, characterized by excellent structural stability, electrical conductivity, and strong interfacial coupling, achieved by assembling carbon-coated MoS_2 nanoplates on carbon-stabilized Ti_3C_2 MXene.[139] The study introduced a carbon nanoplating approach to effectively stabilize metastable MXene, preventing structural degradation and paving the way for MXene-based materials with enhanced properties. The MoS_2/Ti_3C_2 MXene@C electrocatalyst exhibited an overpotential of just 135 mV (Fig. 8e), a low charge-transfer resistance of 1.28 Ω

(Fig. 8f), and outstanding durability. Liu *et al.* developed a nanoroll-like $MoS_2/Ti_3C_2T_x$ hybrid using a liquid nitrogen freezing method followed by annealing.[140] The rapid freezing of a mixture of $Ti_3C_2T_x$ nanosheets and ammonium tetrathiomolybdate induced a sudden strain in $Ti_3C_2T_x$, resulting in a unique nanoroll-shaped hierarchical structure. Annealing in an H_2/Ar atmosphere facilitated the *in situ* formation of vertically aligned MoS_2 crystallites on and within the $Ti_3C_2T_x$ nanorolls (Fig. 8g). This hybrid demonstrated outstanding HER catalytic performance, with a low onset overpotential of 30 mV and 25-fold enhancement in exchange current density compared to pure MoS_2. Meanwhile, Shen *et al.* experimented on the synthesis of a MoS_2 quantum dot (QD) and 2D $Ti_3C_2T_x$ MXene nanosheet.[141] The MoS_2 QDs were uniformly formed *in situ* on the $Ti_3C_2T_x$ nanosheets, while the hybrid retained its layered structure. This MoS_2 QDs/$Ti_3C_2T_x$ catalyst exhibited excellent electrocatalytic activity, achieving a lower overpotential of 220 mV at 10 mA cm^{-2} and a Tafel slope of 72 mV dec^{-1}, attributed to its high conductivity, abundant active sites, and a significant proportion of the 1T metallic phase in the MoS_2 QDs.

4.2.2. MXene/tungsten sulfide composites. WS_2 is another transition metal dichalcogenide, which is often coupled with MXene for a wide range of applications. WS_2 demonstrates exceptional electrochemical activity due to its tunable bandgap, rapid ion/molecule diffusion, readily accessible edge sites, and expansive surface area.[142] However, its poor cycling stability hinders its broader applications. Additionally, WS_2 electrode materials suffer from low specific capacitance, insufficient intrinsic catalytic activity, poor electronic and ionic conductivity, structural degradation, and restricted ion/electron transport.[142] Hussain *et al.* synthesized a porous WS_2 nanosheet-interconnected MXene/GO heterostructure using a hydrothermal method.[100] This heterostructure exhibited low overpotentials of 42 mV and 45 mV with Tafel slopes of 43 mV dec^{-1} and 58 mV dec^{-1} HER in acidic and alkaline media, respectively. The sandwich-like architecture of WS_2@MXene/GO nanocomposites improved electrocatalytic performance by minimizing MXene

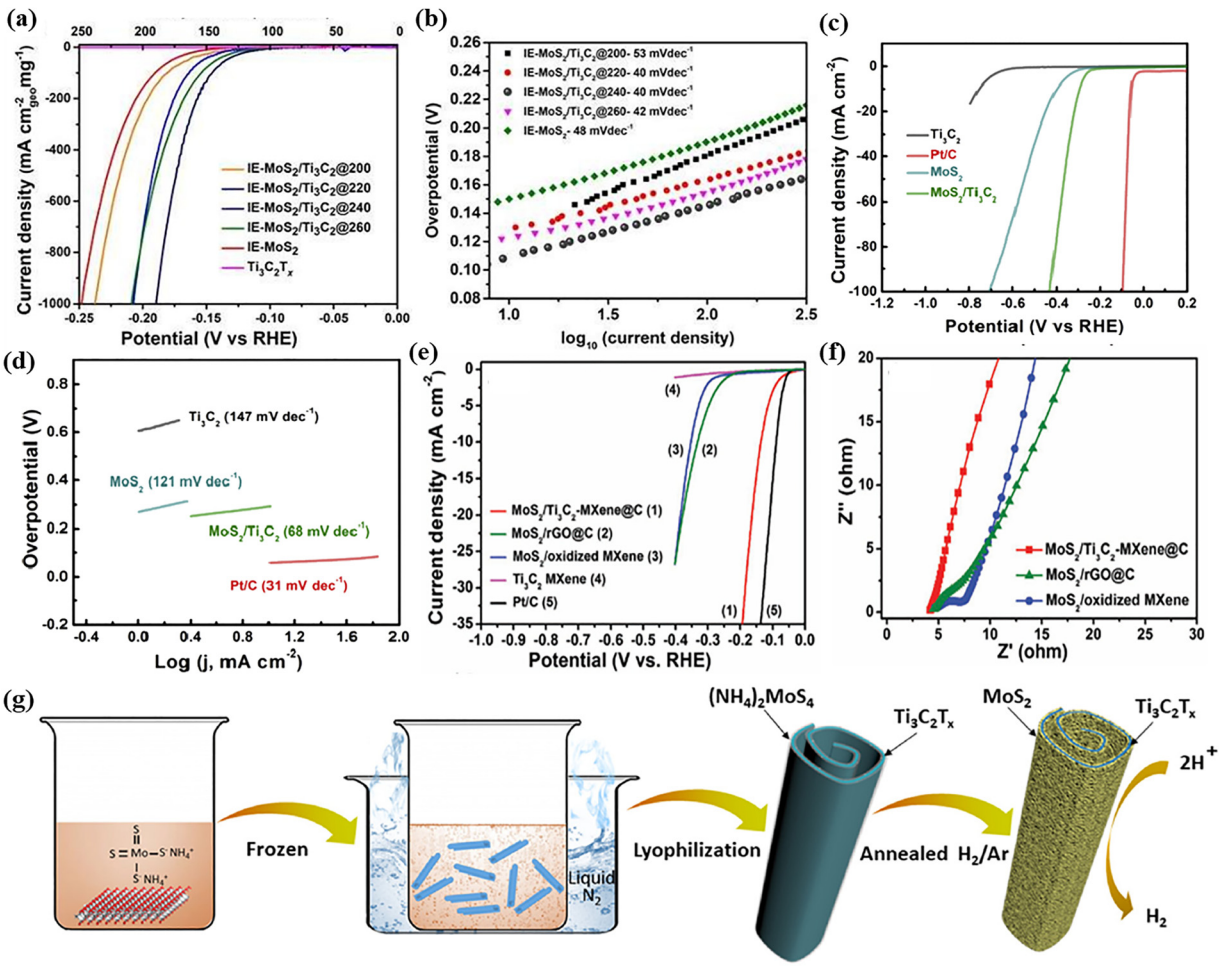

Fig. 8 HER analysis of MoS_2, $Ti_3C_2T_x$, and $MoS_2/Ti_3C_2T_x$ synthesized at different temperatures. Reproduced with permission from ref. 137 copyright 2018, Royal Society of Chemistry. (a) LSV curves (b) Tafel plots, comparative HER study of MoS_2, Ti_3C_2, and MoS_2/Ti_3C_2. Reproduced with permission from ref. 138 copyright 2019, Elsevier. (c) LSV curves (d) Tafel plots, electrochemical HER analysis of MoS_2/Ti_3C_2-MXAene@C, MoS_2/oxidized MXene, MoS_2/rGO@C, and Ti_3C_2 MXene. Reproduced with permission from ref. 139 copyright 2017, John Wiley and Sons. (e) LSV curves (f) EIS spectra (g) Diagrammatic representation nanoroll-like $MoS_2/Ti_3C_2T_x$ synthesis. Reproduced with permission from ref. 140 copyright 2019, Elsevier.

oxidation and aggregation while ensuring adequate exposure of edge sites. Additionally, the porous MXene or GO acted as a conductive substrate, promoting efficient electron transfer. The anchoring of WS_2 on GO/MXene introduced defect-rich active sites and interior voids, enhancing the specific surface area and providing numerous edge sites for long-term stability. DFT analysis revealed that the modified electronic structure of WS_2@MXene/GO achieved a low Gibbs free energy close to the thermoneutral point, significantly boosting HER catalytic activity.

4.2.3. Other MXene/TMS composites. Beyond these, MXenes combined with cobalt, copper, and nickel sulfides have also been investigated for electrochemical water-splitting applications. Han *et al.* achieved efficient interface engineering between MXene and CoS_2 through *in situ* hydrothermal growth followed by sulfurization.[143] The resulting CoS_2@MXene electrocatalyst features a hierarchical structure comprising 1D CoS_2 nanowires and 2D MXene nanosheets, offering a large surface area, abundant active sites, enhanced electron distribution, and robust stability. This design delivers excellent catalytic performance, with a half-wave potential of 0.80 V for ORR, overpotentials of 270 mV and 175 mV for OER and HER at 10 mA cm^{-2}, respectively, and a low overall water-splitting voltage of 1.63 V. These improvements are attributed to: MXene's high electronegativity promoting charge transfer from CoS_2, MXene's conductivity ensuring efficient electron transport, increased active sites, structural stability from the hierarchical design, and enhanced interfacial effects boosting reaction site availability and mass transport. In another study, Sarfraz *et al.* synthesized CuS nanoparticles on HF-free Cl-terminated MXene *via* a hydrothermal process, and it exhibited a HER overpotential of 163 mV and a Tafel slope of 77 mV dec^{-1} at 10 mA cm^{-2}.[144] OER achieved an overpotential of 334 mV at 50 mA cm^{-2} and a Tafel slope of 42 mV dec^{-1}. The CuS/$Ti_3C_2Cl_2$||CuS/$Ti_3C_2Cl_2$ electrolyzer delivered 20 mA cm^{-2} at 1.87 V for overall water splitting and retained 96% of its performance after 48 h at 100 mA cm^{-2}. Recent studies have explored the *in situ* formation of $Ti_3C_2T_x$/Ni_3S_2 nanosheets on 3D nickel foam as a self-supported electrocatalyst for HER in alkaline media.[145] The $Ti_3C_2T_x$/Ni_3S_2/NF catalyst demonstrated exceptional performance, achieving a low overpotential of 72 mV at 10 mA cm^{-2} and a Tafel slope of 45 mV dec^{-1}, indicating efficient charge transfer. This catalyst maintained stable performance for over 12 h without a decline in current density. The 3D porous nickel foam provides a conductive platform and a nickel source for Ni_3S_2 formation, while Ni_3S_2 acts as a spacer to prevent MXene restacking. MXene nanosheets enhance surface roughness, increasing active site availability. To further validate the superior HER performance of $Ti_3C_2T_x$/Ni_3S_2/NF in alkaline media, DFT calculations were performed. The results showed that pristine Ti_3C_2 (ΔG_H = −1.736 eV) and pure Ni_3S_2 (ΔG_H = 1.989 eV) exhibited unfavorable hydrogen adsorption energies, whereas the $Ti_3C_2T_x$/Ni_3S_2 heterostructure displayed a ΔG_H of −0.328 eV, much closer to the ideal value and comparable to Pt (−0.09 eV). This clearly highlights the synergistic effect between $Ti_3C_2T_x$ and NF, where interfacial interactions optimize hydrogen adsorption and thereby account for the experimentally observed enhancement in HER activity.

Iron doping and bimetallic iron–nickel sulfide nanostructures have shown promise in enhancing electronic structure and catalytic performance, though traditional synthesis methods are often complex and limited by poor conductivity. To address these challenges, He *et al.* developed a simple one-pot hydrothermal method to fabricate $FeNi_2S_4$/MXene nanocomposites on Ni–Fe foam.[146] This catalyst demonstrated exceptional performance for both OER and HER, with low overpotentials of 136 mV and 97 mV at 10 mA cm^{-2}, respectively, and high stability. The superior performance is attributed to well-dispersed $FeNi_2S_4$ nanoparticles, enhanced conductivity from $Ti_3C_2T_x$ nanosheets, strong electronic coupling, efficient mass transfer, and a robust hierarchical structure.

4.3. MXene/transition metal selenides composites for overall water splitting

The remarkable conductivity ($\sim 10^3$ S m^{-1}), excellent theoretical specific capacities, and metallic characteristics of transition metal selenides like $NiSe_2$, $CoSe_2$, $MoSe_2$, and $FeSe_2$ make them highly efficient for various applications. These materials are also attractive due to their earth abundance and relatively low cost. MXenes have been combined with transition metal selenides to develop efficient electrocatalysts for overall water splitting.

4.3.1. MXene/molybdenum selenide composites. $MoSe_2$ stands out as a promising candidate due to its unique structure, tunable properties, and low Gibbs free energy. However, its catalytic performance is often limited by its bulk nature, which exposes insufficient active sites for efficient catalytic reactions. Li *et al.* have synthesized a 1T/2H $MoSe_2$/MXene heterostructure through the hydrothermal method.[147] In this composite, MXene acts as a highly conductive substrate, enhancing charge transfer and preventing the aggregation of 1T/2H $MoSe_2$. The $MoSe_2$ component provides abundant active sites, contributing to its excellent electrocatalytic activity. The synergy between the components results in impressive water-splitting performance, with an electrochemically active surface area of 545 cm^2. The composite achieves an overpotential of 95 mV and a Tafel slope of 91 mV dec^{-1} for HER, along with an overpotential of 340 mV and a Tafel slope of 90 mV dec^{-1} for OER. Notably, as a bifunctional electrocatalyst for overall water splitting, it requires only 1.64 V to reach a current density of 10 mA cm^{-2}. Furthermore, the 1T/2H $MoSe_2$/MXene heterostructure demonstrates excellent durability in the water-splitting system.

Previous studies show that Ni doping into $MoSe_2$ improved HER activity compared to pristine $MoSe_2$ due to the lowering of hydrogen binding energy and hydrolytic energy barriers.[148] Building on this principle, Zhong *et al.* incorporated Ni into $MoSe_2$/Ti_2NT_x MXene nanohybrids, enhancing their water splitting performance.[148] The Ni-$MoSe_2$/Ti_2NT_x hybrid achieved an overpotential of 92 mV at 10 mA cm^{-2} and a Tafel slope of 79.7 mV dec^{-1} for HER (Fig. 9a and b), while for OER, it showed

an overpotential of 270 mV at 50 mA cm^{-2} and a Tafel slope of 81.1 mV dec^{-1} (Fig. 9c and d). As a bifunctional electrocatalyst, it required only 1.59 V to deliver 10 mA cm^{-2} in overall water splitting. This superior performance is attributed to the synergistic roles of $MoSe_2$ in regulating hydrolysis sites, Ti_2NT_x as a conductive substrate, and Ni doping in optimizing the electronic structure and facilitating charge transfer.

4.3.2. Other MXene/transition metal selenide composites. Selvam *et al.* synthesized Co-based nanoparticles, including Co(OH)F, CoP, and Co_7Se_8, coupled with exfoliated MXene layers to evaluate their electrocatalytic performance.[149] The exfoliated MXene sheets provided a platform for the growth of 1D Co(OH)F nanorods, which were converted into mesoporous CoP/MXene hybrids through phosphidation and to Co_7Se_8/MXene through selenization. Among these, CoP/MXene demonstrated superior OER activity with a low overpotential of 230 mV at 10 mA cm^{-2} and an overall cell potential of 1.56 V at 10 mA cm^{-2}. The enhanced performance of CoP/MXene is attributed to its abundant active sites, high conductivity, efficient electron transport facilitated by MXene, and mesoporous structure aiding ion diffusion and oxygen release. Additionally, the anion composition significantly influenced catalytic activity and stability. CoP exhibited bifunctional activity and stability for both OER and HER, while CoSe was selectively active for OER but less stable and less effective in HER and bifunctional applications. However, in 2023, Patra *et al.* synthesized a $CoSe_2$/MXene hybrid catalyst using a hydrothermal method, demonstrating remarkable HER.[150] The catalyst achieved an HER overpotential of 230 mV with a Tafel slope of 65 mV dec^{-1} (Fig. 9e and f), along with low charge transfer resistance,

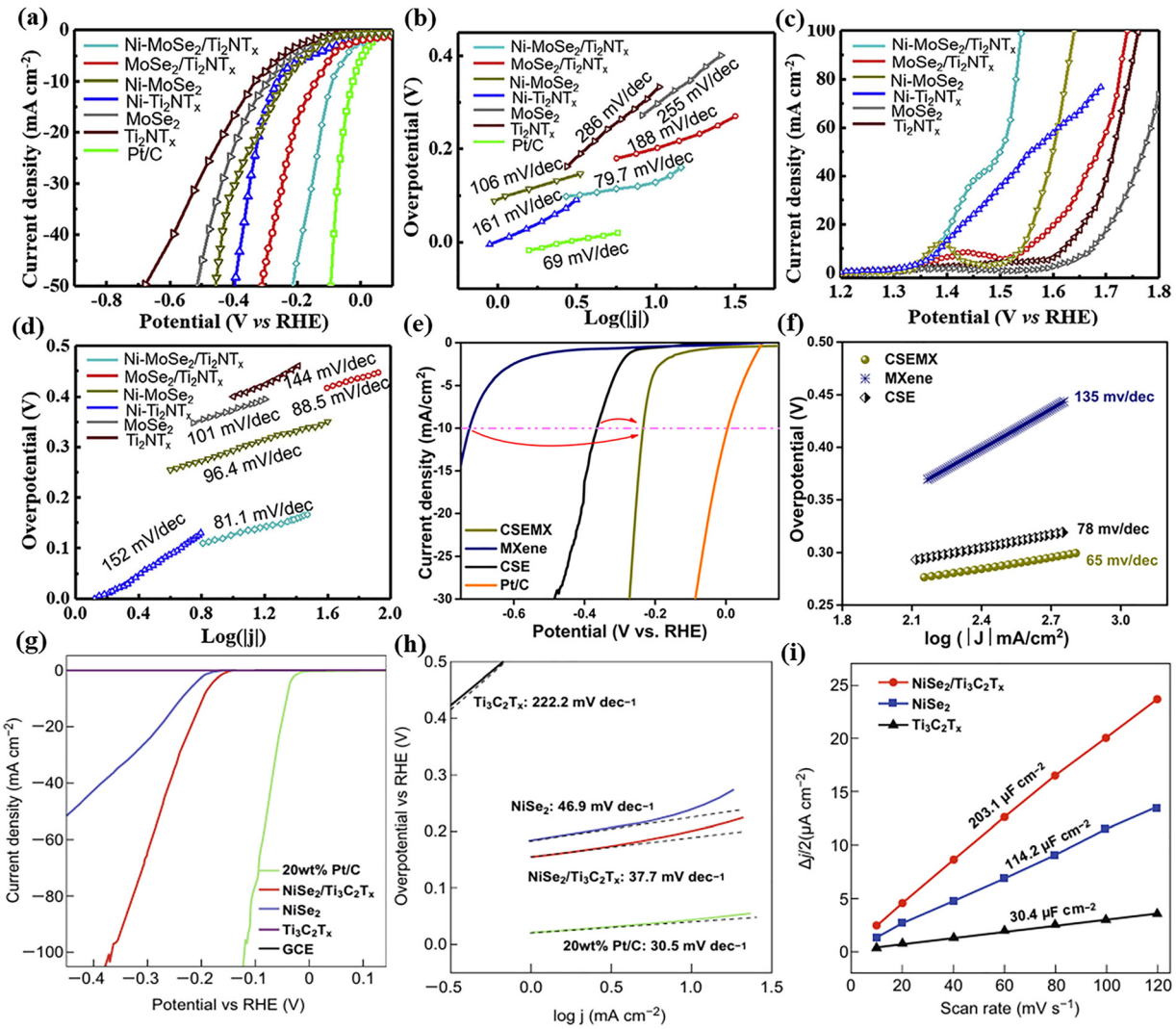

Fig. 9 Overall water splitting analysis of Ni-$MoSe_2$/Ti_2NT_x, $MoSe_2$, Ti_2NT_x, Ni-$MoSe_2$, Ni-Ti_2NT_x and $MoSe_2$/Ti_2NT_x. Reproduced with permission from ref. 148 copyright 2020, Elsevier. (a) LSV for HER (b) Tafel slope for HER (c) LSV for OER (d) Tafel slope for OER, HER analysis of $CoSe_2$/MXene, $CoSe_2$ and MXene. Reproduced with permission from ref. 150 copyright 2023, Elsevier. (e) LSV curve (f) Tafel slope, comparative HER analysis of $NiSe_2$, $NiSe_2$/$Ti_3C_2T_x$ hybrid, and $Ti_3C_2T_x$. Reproduced with permission from ref. 151 copyright 2019, Springer Nature. (g) LSV curves (h) Tafel plots (i) double-layer capacitances.

enhanced charge transport pathways, abundant electrochemically active sites, a larger surface area, and improved H^+ adsorption energy, making it an exceptional electrocatalyst for HER applications. The $CoSe_2$ decoration on MXene provided additional active sites and expanded interlayer spacing for efficient ion penetration. Meanwhile, MXene's conductive framework facilitated smooth charge transfer and ensured material stability. The synergy between $CoSe_2$ and MXene further enhanced catalytic activity by providing a high surface area, reduced energy barrier, and lower contact resistance.

$NiSe_2$ is another transition metal diselenide that gained attention due to its distinctive electronic structure and ability to exhibit multiple oxidation states.[152] However, pristine $NiSe_2$ suffers from drawbacks like insufficient cycling stability, poor electrical conductivity, and a deficiency in electrochemically active sites.[152] To overcome these limitations, hybridizing $NiSe_2$ with other materials has proven to be a promising approach. The $NiSe_2/Ti_3C_2T_x$ hybrid showed excellent HER performance with a low overpotential of 200 mV and a Tafel slope of 37.7 mV dec^{-1}, indicating efficient reaction kinetics (Fig. 9g and h).[151] Its double-layer capacitance (203.1 μF cm^{-2}) significantly exceeded that of unmodified $NiSe_2$ (114.2 μF cm^{-2}), highlighting improved charge transfer and better utilization of active sites due to $Ti_3C_2T_x$ wrapping (Fig. 9i). These enhancements were attributed to the high conductivity and strong chemical coupling between $Ti_3C_2T_x$ and $NiSe_2$. Meanwhile, Chaudhary *et al.* developed novel 3D Ti_3C_2 MXene/rGO composite aerogels coupled with octahedral $NiSe_2$ at varying MXene loading.[153] The aerogels formed a cellular lattice-like structure, enhancing contact with the electrolyte, boosting ion diffusion, and enabling fast charge transport. The optimized electrode achieved low overpotentials of 97 mV and 262 mV to reach 10 mA cm^{-2} for both HER and OER, respectively, with lower Tafel slopes. The robust aerogel framework prevented $NiSe_2$ aggregation, buffered volume changes, and maintained structural integrity during prolonged use.

4.4. MXene/transition metal tellurides composites for overall water splitting

Studies show that the anion serves as the active site in dichalcogenides for HER. Since tellurium has a lower electronegativity (2.1 eV) compared to other chalcogens such as sulfur (2.58 eV) and selenium (2.55 eV), transition metal tellurides exhibit a higher degree of covalency than other transition metal dichalcogenides.[154] Transition metal tellurides, having lower electronegativity, exhibit weaker H_2 desorption strength and better electrocatalytic performance for HER.[154] Samal *et al.* synthesized $CoTe_2/Ti_3C_2T_x$ and $NiTe_2/Ti_3C_2T_x$ composites using a hydrothermal method and evaluated their electrocatalytic performance for water splitting.[154] Among the two, $CoTe_2/Ti_3C_2T_x$ demonstrated superior efficiency with a lower overpotential of 200 mV and a Tafel slope of 95 mV dec^{-1} for HER compared to $NiTe_2/Ti_3C_2T_x$. The enhanced electrochemical and catalytic performance of $CoTe_2/Ti_3C_2T_x$ was attributed to its enhanced surface area, efficient charge transfer pathways, the role of valence electrons in metal ions, and well-optimized active sites. This approach of integrating telluride systems with MXene opens new possibilities for exploring their potential in advanced applications. Table 2 summarizes the overall water splitting efficiency of MXene/TMO and MXene/TMC composites.

From these studies, it is evident that transition metal oxides and chalcogenides integrated with MXenes represent an

Table 2 The overall water splitting efficiency of MXene/TMO and MXene/TMC composites

Composite	Synthesis	HER overpotential @10 mA cm^{-2}	Electrolyte	Ref.
Co_3O_4/2D Ti_3C_2	Solvothermal	300 mV	1 M KOH	116
Co–CoO/Ti_3C_2	Electrostatic assembly & reduction	45 mV	1 M KOH	118
Ti_3C_2@MoO_3	Hydrothermal	190 mV	1 M KOH	122
Na-MnO_{2-x}/Ti_3C_2	Electrodeposition	439.7 mV	PVA:Na_2SO_4	123
d-Ti_3C_2/V_2O_5	Hydrothermal	90 mV	1 M KOH	124
Ru- RuO_2/MXene@CC	Hydrothermal	43 mV	1 M KOH	125
$NiFe_2O_4/Ti_3C_2$	Hydrothermal	173 mV	0.5 M KOH	129
$CoNiFe_2O_4$/MXene	Layer-by-layer assembly	17 mV	1 M KOH	130
$RuCo_2O_4$@$Ti_3C_2T_x$@NF	Electrodeposition	68 mV	1 M KOH	131
$CuCo_2O_4/Ti_3C_2T_x$	Solvothermal & annealing	360 mV	1 M KOH	132
$MnCo_2O_4/Ti_3C_2T_x$	Hydrothermal	51 mV	0.5 M H_2SO_4	133
$MoS_2 \perp Ti_3C_2$	Microwave-assisted colloidal synthesis	95 mV	0.5 M H_2SO_4	137
MoS_2/Ti_3C_2	Hydrothermal	280 mV	0.5 M H_2SO_4	138
MoS_2/Ti_3C_2–MXene@C	Carbon nanoplating & hydrothermal	135 mV	0.5 M H_2SO_4	139
$MoS_2/Ti_3C_2T_x$	Liquid nitrogen freezing & annealing	152 mV	0.5 M H_2SO_4	140
MoS_2 QDs/$Ti_3C_2T_x$	Solvothermal	220 mV	0.5 M H_2SO_4	141
WS_2/MXene/GO	Hydrothermal	42 mV	0.5 M H_2SO_4	100
CoS_2@MXene	Hydrothermal	175 mV	1 M KOH	143
CuS/$Ti_3C_2Cl_2$	Hydrothermal	163 mV	1 M KOH	144
$Ti_3C_2T_x/Ni_3S_2$	Hydrothermal	72 mV	1 M KOH	145
$FeNi_2S_4$/MXene	Hydrothermal	97 mV	1 M KOH	146
1T/2H $MoSe_2$/MXene	Hydrothermal	95 mV	1 M KOH	147
Ni-$MoSe_2/Ti_2NT_x$	Hydrothermal	92 mV	1 M KOH	148
$CoSe_2$/MXene	Hydrothermal	230 mV	0.5 M H_2SO_4	150
$NiSe_2/Ti_3C_2T_x$	Hydrothermal	200 mV	0.5 M H_2SO_4	151
$NiSe_2/Ti_3C_2$/rGO	Hydrothermal	97 mV	1 M KOH	153

advanced approach for water-splitting applications, effectively utilizing the complementary properties of these materials.

5. Conclusion and future perspectives

This review highlights the significance of MXene-based composites with TMDs and TMOs in addressing global energy challenges. Beginning with the relevance of sustainable development goals, it emphasizes the urgent need for efficient and renewable energy storage and conversion technologies. The discussion then underscores the unique properties of MXenes, TMDs, and TMOs, which make them promising candidates for electrochemical applications. The electrochemical performance of MXene/TMD and MXene/TMO hybrids in supercapacitors and electrocatalytic water splitting is systematically analyzed. The synergistic interactions between MXene and its hybrid components contribute to enhanced charge storage, improved rate capability, and cycling stability in supercapacitors. Similarly, in water splitting, these composites exhibit remarkable catalytic activity, lowering overpotentials and improving reaction kinetics. The review includes tables summarizing various MXene/TMO and MXene/TMD hybrid electrodes employed in supercapacitors and water splitting, demonstrating their synergistic effects. Notably, Mn-based MXene/TMO composites have been widely explored due to their high theoretical capacitance, where porous architectures and large surface areas significantly enhance faradaic reactions. In water splitting, MXene's surface chemistry plays a crucial role in catalytic performance, while TMDs have proven to be highly efficient bifunctional catalysts.

Despite these advancements, several challenges must be addressed for further improvement.

• To date, MXene is majorly synthesized using fluorine containing etchants, which pose significant risks to both health and the environment. Additionally, these etchants hinder the large-scale production of MXene. Most research has centred around MXene-based electrocatalysts derived from fluorine-mediated methods. Therefore, there is an urgent need to develop and advance MXene-based electrocatalysts through greener synthetic approaches.

• More than 100 MXene compositions have been theoretically predicted, yet only a limited number have been successfully synthesized and studied for electrocatalytic applications. This underscores the need to intensify research efforts to realize the predicted MXenes and evaluate their electrocatalytic potential.

• The stability of MXene-based composites in electrochemical processes is a major challenge, as the active sites with high surface area are prone to corrosion in strong alkaline electrolytes. Enhancing structural stability and durability is crucial for their long-term efficiency in electrocatalytic applications.

• Most studies on MXene-based hybrids for water splitting and supercapacitors focus on pre- and post-reaction analyses, lacking *in situ* characterization. Advanced *in situ* techniques are needed to reveal surface changes, active sites, and catalytic mechanisms.

• It is essential to define the important electrochemical properties, including electron transfer, ionic and charge transport, conductivity, and capacitance, while also exploring effective strategies to harness the electrochemistry of MXenes with a focus on mechanistic aspects.

• The large-scale production of MXenes and their heterostructures poses a challenge but also offers a promising opportunity for further development.

• 3D MXene/TMO or MXene/TMD heterostructures hold great potential for energy storage devices, as their diverse compositions and morphologies can enhance ion diffusion and increase reactive sites. Further research on these composites should be strengthened to optimise their potential fully.

• More electrocatalytic experiments on energy storage and conversion should be conducted in various electrolytes, including organic, ionic liquid, water-in-salt, and mixed-ion electrolytes.

• A key challenge lies in identifying the most effective MXene/TMO and MXene/TMC combinations for different energy storage devices. Computational modeling and theoretical studies can help pre-screen candidates and provide insights into ion dynamics within heterostructures.

• The design of three-dimensional MXene/TMO and MXene/TMC heterostructures with varied terminal groups and compositions could enhance ion diffusion pathways and increase the availability of reactive sites.

• The relatively low energy density of supercapacitors remains a significant challenge. Although MXenes exhibit high capacitance, their energy density is restricted by the narrow electrochemically stable voltage window caused by irreversible anodic oxidation. To overcome this limitation, both structural design and electrochemical modifications can be employed to enhance performance. One promising approach is the partial oxidation of MXenes to generate oxide nanostructures, thereby increasing the overall capacity of MXene-based electrodes.

• Theoretical studies often rely on oversimplified models due to computational limitations, leading to overly optimistic predictions. To bridge this gap, methodologies for synthesizing well-defined MXene hybrids must be developed and their performance should be rigorously tested. In-depth investigations of their surface chemistry and electrochemical mechanisms should integrate both theoretical and experimental approaches using advanced *in situ* techniques. Refining theoretical models through such studies will enhance their accuracy. Additionally, machine learning can aid in screening compositions, surfaces, and crystal structures for various applications.

Addressing these limitations through innovative material design and advanced characterization techniques will be crucial for the practical deployment of MXene-based hybrids in next-generation energy storage and conversion systems.

Author contributions

Sandra Mathew: conceptualization, investigation, formal analysis, data curation, and writing original draft. Kalathiparambil

Rajendra Pai Sunajadevi: supervision, conceptualization, writing, review, and editing, Dephan Pinheiro: writing, review, and editing.

Conflicts of interest

There are no conflicts to declare.

Data availability

No primary research results, software or code have been included and no new data were generated or analysed as part of this review.

Acknowledgements

The authors are grateful to Christ University, Bangalore, for their support and encouragement.

References

1 O. O. Volkova, V. Skorb and D. G. Shchukin, *Mater. Adv.*, 2024, **5**, 394–408.
2 A. M. Omer, *Renewable Sustainable Energy Rev.*, 2008, **12**, 2265–2300.
3 W. Schramade, *J. Appl. Corp. Financ.*, 2017, **29**, 87–99.
4 L. Wang, Y. Zhang, L. Chen, H. Xu and Y. Xiong, *Adv. Mater.*, 2018, **30**, 1–12.
5 H. Sun, X. Xu, H. Kim, Z. Shao and W. Jung, *InfoMat*, 2024, **6**(1), e12494.
6 S. A. Sherif, F. Barbir and T. N. Veziroglu, *Sol. Energy*, 2005, **78**, 647–660.
7 H. Sun, X. Xu, H. Kim, W. Jung, W. Zhou and Z. Shao, *Energy Environ. Mater.*, 2023, **6**, 1–21.
8 L. Quan, H. Jiang, G. Mei, Y. Sun and B. You, *Chem. Rev.*, 2024, **124**, 3694–3812.
9 M. Z. Abid, K. Rafiq, A. Rauf, R. H. Althomali and E. Hussain, *Mater. Adv.*, 2024, **5**, 2238–2252.
10 Z. Li, L. Sun, Y. Zhang, Y. Han, W. Zhuang, L. Tian and W. Tan, *Coord. Chem. Rev.*, 2024, **510**, 215837.
11 M. Khalil, M. Lesa, A. G. Juandito, A. R. Sanjaya, T. A. Ivandini and G. T. M. Kadja, *Mater. Adv.*, 2023, **4**, 3853–3862.
12 Reenu, Sonia, L. Phor, A. Kumar and S. Chahal, *J. Energy Storage*, 2024, **84**, 110698.
13 K. Dissanayake and D. Kularatna-Abeywardana, *J. Energy Storage*, 2024, **96**, 112563.
14 R. Swaminathan, P. Pazhamalai, K. Krishnamoorthy, V. Natraj, V. Krishnan and S.-J. Kim, *J. Energy Storage*, 2024, **83**, 110642.
15 P. K. Ray and K. Parida, *Mater. Adv.*, 2025, **6**, 84–116.
16 B. S. Ammaiyappan, *ICAMMS 2024. Sustainable Civil Infrastructures*. Springer, Cham. Springer, 2024, pp. 365–378.
17 S. Jayakumar, P. C. Santhosh, S. Ramakrishna and A. V. Radhamani, *J. Energy Storage*, 2024, **97**, 112741.
18 M. M. Tunesi, R. A. Soomro, X. Han, Q. Zhu, Y. Wei and B. Xu, *Nano Converg.*, 2021, **8**, 5.
19 S. Vigneshwaran, P. Karthikeyan, C. Min and S. Meenakshi, *J. Environ. Manage.*, 2020, **273**, 111125.
20 Z. Ud, D. Babar and B. Della Ventura, *RSC Adv.*, 2022, **12**, 19590–19610.
21 V. Shukla, *Mater. Adv.*, 2020, **1**, 3104–3121.
22 Md. Ahmaruzzaman, *RSC Adv.*, 2022, **12**, 34766–34789.
23 M. Mozafari and M. Soroush, *Mater. Adv.*, 2021, **2**, 7277–7307.
24 G. Manasa and C. S. Rout, *Mater. Adv.*, 2024, **5**, 83–122.
25 R. A. Chavan, D. M. Ulisso, A. S. Rasal and Y. Chang, *Mater. Adv.*, 2023, **4**, 2659–2666.
26 W. Hong, B. C. Wyatt, S. K. Nemani and B. Anasori, *MRS Bull.*, 2020, **45**, 850–861.
27 S. Mathew, K. R. P. Sunajadevi, D. Pinheiro and M. Selvaraj, *Int. J. Hydrogen Energy*, 2025, **112**, 189–197.
28 S. Iravani and R. S. Varma, *Mater. Adv.*, 2023, **4**, 4317–4332.
29 S. Li, E. Li, X. An, X. Hao, Z. Jiang and G. Guan, *Nanoscale*, 2021, **13**, 12788–12817.
30 J. Huang, Y. Jiang, T. An and M. Cao, *J. Mater. Chem. A*, 2020, **8**, 25465–25498.
31 K. C. Majhi and M. Yadav, *ACS Eng. Au*, 2023, **3**, 278–284.
32 N. S. Hassan, A. A. Jalil, N. F. Khusnun, A. Ahmad, T. A. T. Abdullah, R. M. Kasmani, N. Norazahar, M. F. A. Kamaroddin and D. V. N. Vo, *Environ. Chem. Lett.*, 2022, **20**, 311–333.
33 A. Kumar, H. K. Rathore, D. Sarkar and A. Shukla, *Electrochem. Sci. Adv.*, 2022, **2**(6), e210018.
34 Y. Ma, X. Xie, W. Yang, Z. Yu, X. Sun, Y. Zhang, X. Yang, H. Kimura, C. Hou, Z. Guo and W. Du, *Adv. Compos. Hybrid Mater.*, 2021, **4**, 906–924.
35 S. Mathew and S. Devi, *Int. J. Hydrogen Energy*, 2024, **71**, 1283–1292.
36 S. Mathew and S. Devi, *Colloids Surf., A*, 2024, **684**, 133170.
37 Y. Tian, C. Yang, W. Que, X. Liu, X. Yin and L. B. Kong, *J. Power Sources*, 2017, **359**, 332–339.
38 H. Jiang, Z. Wang, Q. Yang, M. Hanif, Z. Wang, L. Dong and M. Dong, *Electrochim. Acta*, 2018, **290**, 695–703.
39 A. Amiri, Y. Chen, C. Bee Teng and M. Naraghi, *Energy Storage Mater.*, 2020, **25**, 731–739.
40 P. Lian, Y. Dong, Z.-S. Wu, S. Zheng, X. Wang, S. Wang, C. Sun, J. Qin, X. Shi and X. Bao, *Nano Energy*, 2017, **40**, 1–8.
41 M. Jiang, D. Wang, Y. Kim, C. Duan, D. V. Talapin and C. Zhou, *Angew. Chem.*, 2024, **63**(37), e202409480.
42 J. Yan, Z. Fan, T. Wei, W. Qian, M. Zhang and F. Wei, *Carbon*, 2010, **48**, 3825–3833.
43 H. Zhou, Y. Lu, F. Wu, L. Fang, H. Luo, Y. Zhang and M. Zhou, *J. Alloys Compd.*, 2019, **802**, 259–268.
44 H. Peçenek, S. Yetiman, F. K. Dokan, M. S. Onses, E. Yılmaz and E. Sahmetlioglu, *Ceram. Int.*, 2022, **48**, 7253–7260.
45 Z. A. Sheikh, P. K. Katkar, H. Kim, S. Rehman, K. Khan, V. D. Chavan, R. Jose, M. F. Khan and D. Kee Kim, *J. Energy Storage*, 2023, **71**, 107997.

46 E. Hayashi, Y. Yamaguchi, K. Kamata, N. Tsunoda, Y. Kumagai, F. Oba and M. Hara, *J. Am. Chem. Soc.*, 2019, **141**, 890–900.
47 J.-G. Wang, F. Kang and B. Wei, *Prog. Mater. Sci.*, 2015, **74**, 51–124.
48 Q. Wang, Z. Zhang, Z. Zhang, X. Zhou and G. Ma, *J. Solid State Electrochem.*, 2019, **23**, 361–365.
49 W. Yuan, L. Cheng, B. Zhang and H. Wu, *Ceram. Int.*, 2018, **44**, 17539–17543.
50 S. Chen, Y. Xiang, W. Xu and C. Peng, *Inorg. Chem. Front.*, 2019, **6**, 199–208.
51 J. Zhou, J. Yu, L. Shi, Z. Wang, H. Liu, B. Yang, C. Li, C. Zhu and J. Xu, *Small*, 2018, **14**, 1803786.
52 R. B. Rakhi, B. Ahmed, D. Anjum and H. N. Alshareef, *ACS Appl. Mater. Interfaces*, 2016, **8**, 18806–18814.
53 Q. Liu, J. Yang, X. Luo, Y. Miao, Y. Zhang, W. Xu, L. Yang, Y. Liang, W. Weng and M. Zhu, *Ceram. Int.*, 2020, **46**, 11874–11881.
54 X. Li, Z. Lin, Y. Wei, W. Luo, J. Ding, T. Li and Y. Ma, *J. Energy Storage*, 2022, **55**, 105668.
55 K. O. Oyedotun, D. Y. Momodu, M. Naguib, A. A. Mirghni, T. M. Masikhwa, A. A. Khaleed, M. Kebede and N. Manyala, *Electrochim. Acta*, 2019, **301**, 487–499.
56 V. D. Nithya and N. S. Arul, *J. Power Sources*, 2016, **327**, 297–318.
57 Y. Gao, D. Wu, T. Wang, D. Jia, W. Xia, Y. Lv, Y. Cao, Y. Tan and P. Liu, *Electrochim. Acta*, 2016, **191**, 275–283.
58 H. Quan, B. Cheng, Y. Xiao and S. Lei, *Chem. Eng. J.*, 2016, **286**, 165–173.
59 R. Zou, H. Quan, M. Pan, S. Zhou, D. Chen and X. Luo, *Electrochim. Acta*, 2018, **292**, 31–38.
60 T.-Z. Shi, Y.-L. Feng, T. Peng and B.-G. Yuan, *Electrochim. Acta*, 2021, **381**, 138245.
61 Y. Ma, H. Sheng, W. Dou, Q. Su, J. Zhou, E. Xie and W. Lan, *ACS Appl. Mater. Interfaces*, 2020, **12**, 41410–41418.
62 H. Li, Y. Liu, S. Lin, H. Li, Z. Wu, L. Zhu, C. Li, X. Wang, X. Zhu and Y. Sun, *J. Power Sources*, 2021, **497**, 229882.
63 W. Liang and I. Zhitomirsky, *Materials*, 2021, **14**, 2930.
64 T. Arun, A. Mohanty, A. Rosenkranz, B. Wang, J. Yu, M. J. Morel, R. Udayabhaskar, S. A. Hevia, A. Akbari-Fakhrabadi, R. V. Mangalaraja and A. Ramadoss, *Electrochim. Acta*, 2021, **367**, 137473.
65 A. Ihsan, S. T. Almutairi, H. M. A. Mahmoud, M. F. Warsi and S. Munir, *Ceram. Int.*, 2023, **49**, 37650–37660.
66 Y. Yang, F. Yang, H. Hu, S. Lee, Y. Wang, H. Zhao, D. Zeng, B. Zhou and S. Hao, *Chem. Eng. J.*, 2017, **307**, 583–592.
67 R. Ramachandran, C. Zhao, M. Rajkumar, K. Rajavel, P. Zhu, W. Xuan, Z.-X. Xu and F. Wang, *Electrochim. Acta*, 2019, **322**, 134771.
68 Q. X. Xia, J. Fu, J. M. Yun, R. S. Mane and K. H. Kim, *RSC Adv.*, 2017, **7**, 11000–11011.
69 K. Zhang, G. Ying, L. Liu, F. Ma, L. Su, C. Zhang, D. Wu, X. Wang and Y. Zhou, *Materials*, 2019, **12**, 188.
70 J. Zhu, Y. Tang, C. Yang, F. Wang and M. Cao, *J. Electrochem. Soc.*, 2016, **163**, A785–A791.
71 J. Zhao, F. Liu and W. Li, *Nanomaterials*, 2019, **9**, 377.
72 J. Yu, M. Zeng, J. Zhou, H. Chen, G. Cong, H. Liu, M. Ji, C. Zhu and J. Xu, *Chem. Eng. J.*, 2021, **426**, 130765.
73 X. Lu, J. Zhu, W. Wu and B. Zhang, *Electrochim. Acta*, 2017, **228**, 282–289.
74 Z. Gui, E. Gillette, J. Duay, J. Hu, N. Kim and S. B. Lee, *Phys. Chem. Chem. Phys.*, 2015, **17**, 15173–15180.
75 J. Y. Hwang, M. F. El-Kady, Y. Wang, L. Wang, Y. Shao, K. Marsh, J. M. Ko and R. B. Kaner, *Nano Energy*, 2015, **18**, 57–70.
76 Y. Zhu, X. Ji, C. Pan, Q. Sun, W. Song, L. Fang, Q. Chen and C. E. Banks, *Energy Environ. Sci.*, 2013, **6**, 3665.
77 C. Zhang, H. Zhou, X. Yu, D. Shan, T. Ye, Z. Huang and Y. Kuang, *RSC Adv.*, 2014, **4**, 11197.
78 H. Li, X. Li, J. Liang and Y. Chen, *Adv. Energy Mater.*, 2019, **9**, 1803987.
79 R. Liu, A. Zhang, J. Tang, J. Tian, W. Huang, J. Cai, C. Barrow, W. Yang and J. Liu, *Chem. – Eur. J.*, 2019, **25**, 5547–5554.
80 W. Luo, Y. Sun, Z. Lin, X. Li, Y. Han, J. Ding, T. Li, C. Hou and Y. Ma, *J. Energy Storage*, 2023, **62**, 106807.
81 S. B. Ambade, R. B. Ambade, W. Eom, S. H. Noh, S. H. Kim and T. H. Han, *Adv. Mater. Interfaces*, 2018, **5**, 1–11.
82 C. Peng, Z. Kuai, T. Zeng, Y. Yu, Z. Li, J. Zuo, S. Chen, S. Pan and L. Li, *J. Alloys Compd.*, 2019, **810**, 151928.
83 C. Cui, J. Xu, L. Wang, D. Guo, M. Mao, J. Ma and T. Wang, *ACS Appl. Mater. Interfaces*, 2016, **8**, 8568–8575.
84 C. Guan, X. Liu, W. Ren, X. Li, C. Cheng and J. Wang, *Adv. Energy Mater.*, 2017, **7**, 1–8.
85 C. Chen, D. Yan, X. Luo, W. Gao, G. Huang, Z. Han, Y. Zeng and Z. Zhu, *ACS Appl. Mater. Interfaces*, 2018, **10**, 4662–4671.
86 Y. Wang, J. Sun, X. Qian, Y. Zhang, L. Yu, R. Niu, H. Zhao and J. Zhu, *J. Power Sources*, 2019, **414**, 540–546.
87 J. Song, P. Hu, Y. Liu, W. Song and X. Wu, *ChemistrySelect*, 2019, **4**, 12886–12890.
88 X. Zhang, B. Shao, A. Guo, Z. Gao, Y. Qin, C. Zhang, F. Cui and X. Yang, *J. Alloys Compd.*, 2021, **862**, 158546.
89 X. Liu, F. Xu, Z. Li, Z. Liu, W. Yang, Y. Zhang, H. Fan and H. Y. Yang, *Coord. Chem. Rev.*, 2022, **464**, 214544.
90 M. A. Kosnan, M. A. Azam, N. E. Safie, R. F. Munawar and A. Takasaki, *Micromachines*, 2022, **13**, 1837.
91 X. Wang, H. Li, H. Li, S. Lin, W. Ding, X. Zhu, Z. Sheng, H. Wang, X. Zhu and Y. Sun, *Adv. Funct. Mater.*, 2020, **30**, 1–11.
92 M. Chandran, A. Thomas, A. Raveendran, M. Vinoba and M. Bhagiyalakshmi, *J. Energy Storage*, 2020, **30**, 101446.
93 C. Ouyang, X. Wang, C. Wang, X. Zhang, J. Wu, Z. Ma, S. Dou and S. Wang, *Electrochim. Acta*, 2015, **174**, 297–301.
94 S. F. Niu and J. H. Zheng, *J. Alloys Compd.*, 2018, **737**, 809–814.
95 Y. Zhao, J. Guo, A. Liu and T. Ma, *J. Alloys Compd.*, 2020, **814**, 152271.
96 Y. Luo, C. Yang, Y. Tian, Y. Tang, X. Yin and W. Que, *J. Power Sources*, 2020, **450**, 227694.
97 X. Liu, F. Xu, Z. Li, Z. Liu, W. Yang, Y. Zhang, H. Fan and H. Y. Yang, *Coord. Chem. Rev.*, 2022, **464**, 214544.

98 H. Liu, R. Hu, J. Qi, Y. Sui, Y. He, Q. Meng, F. Wei, Y. Ren, Y. Zhao and W. Wei, *Adv. Mater. Interfaces*, 2020, **7**, 1901659.
99 J. Vyskočil, C. C. Mayorga-Martinez, K. Szőkölová, A. Dash, J. Gonzalez-Julian, Z. Sofer and M. Pumera, *ChemElectroChem*, 2019, **6**, 3982–3986.
100 S. Hussain, D. Vikraman, Z. Ali Sheikh, M. Taqi Mehran, F. Shahzad, K. Mujasam Batoo, H.-S. Kim, D.-K. Kim, M. Ali and J. Jung, *Chem. Eng. J.*, 2023, **452**, 139523.
101 M. Yan, Y. Yao, J. Wen, L. Long, M. Kong, G. Zhang, X. Liao, G. Yin and Z. Huang, *ACS Appl. Mater. Interfaces*, 2016, **8**, 24525–24535.
102 X. Chen, D. Chen, X. Guo, R. Wang and H. Zhang, *ACS Appl. Mater. Interfaces*, 2017, **9**, 18774–18781.
103 H. Li, X. Chen, E. Zalnezhad, K. N. Hui, K. S. Hui and M. J. Ko, *J. Ind. Eng. Chem.*, 2020, **82**, 309–316.
104 W. Wu, C. Zhao, J. Zhu, D. Niu, D. Wei, C. Wang, F. Wang and L. Wang, *Ceram. Int.*, 2020, **46**, 12200–12208.
105 X. He, T. Bi, X. Zheng, W. Zhu and J. Jiang, *Electrochim. Acta*, 2020, **332**, 135514.
106 W. Wu, D. Niu, J. Zhu, Y. Gao, D. Wei, C. Zhao, C. Wang, F. Wang, L. Wang and L. Yang, *Ceram. Int.*, 2019, **45**, 16261–16269.
107 J. Xu, X. Yang, Y. Zou, L. Zhu, F. Xu, L. Sun, C. Xiang and J. Zhang, *J. Alloys Compd.*, 2022, **891**, 161945.
108 M. Sajjad, M. Amin, M. S. Javed, M. Imran, W. Hu, Z. Mao and W. Lu, *J. Energy Storage*, 2021, **43**, 103176.
109 H. Jiang, Z. Wang, Q. Yang, L. Tan, L. Dong and M. Dong, *Nano-Micro Lett.*, 2019, **11**, 31.
110 S. Hussain, I. Rabani, D. Vikraman, T. Mehran, F. Shahzad, Y. Seo, H. Kim and J. Jung, *Int. J. Energy Res.*, 2021, **45**, 18770–18785.
111 S. Hussain, D. Vikraman, M. T. Mehran, M. Hussain, G. Nazir, S. A. Patil, H.-S. Kim and J. Jung, *Renewable Energy*, 2022, **185**, 585–597.
112 J. Wang, G. Li, G. Xie, Z. Huang, P. Zhang, B. Xu, X. Xie and N. Zhang, *SusMat*, 2024, **4**, 1–13.
113 J. Wang, G. Xie, S. Zhang, G. Li, Z. Huang, X. Li, X. Xie and N. Zhang, *J. Colloid Interface Sci.*, 2025, **685**, 724–732.
114 X. Xu, D. Feng, L. You, Y. Xie, F. Wu, Y. Zhu, Y. Mei and D. Xie, *Energy Mater. Adv.*, 2024, **5**, 0146.
115 L. Liu, Z. Jiang, L. Fang, H. Xu, H. Zhang, X. Gu and Y. Wang, *ACS Appl. Mater. Interfaces*, 2017, **9**, 27736–27744.
116 Y. Lu, D. Fan, Z. Chen, W. Xiao, C. Cao and X. Yang, *Sci. Bull.*, 2020, **65**, 460–466.
117 A. Sunny, S. Rajalekshmi and A. Pandikumar, *J. Alloys Compd.*, 2024, **1003**, 175532.
118 D. Guo, X. Li, Y. Jiao, H. Yan, A. Wu, G. Yang, Y. Wang, C. Tian and H. Fu, *Nano Res.*, 2022, **15**, 238–247.
119 A. Manikandan, P. R. Ilango, C.-W. Chen, Y.-C. Wang, Y.-C. Shih, L. Lee, Z. M. Wang, H. Ko and Y.-L. Chueh, *J. Mater. Chem. A*, 2018, **6**, 15320–15329.
120 L. Li, T. Zhang, J. Yan, X. Cai and S. (Frank) Liu, *Small*, 2017, **13**(25), 1700441.
121 M. Li, R. Sun, Y. Li, J. Jiang, W. Xu, H. Cong and S. Han, *Chem. Eng. J.*, 2022, **431**, 133941.
122 I. Ashraf, S. Ahmad, S. Rizwan and M. Iqbal, *Fuel*, 2021, **299**, 120928.
123 B. Thanigai Vetrikarasan, A. R. Nair, S. K. Shinde, D.-Y. Kim, J. M. Kim, R. N. Bulakhe, S. N. Sawant and A. D. Jagadale, *J. Energy Storage*, 2024, **94**, 112457.
124 I. Ashraf, S. Ahmad, F. Nazir, D. Dastan, Z. Shi, H. Garmestani and M. Iqbal, *Int. J. Hydrogen Energy*, 2022, **47**, 27383–27396.
125 X. Shi, M. Du, H. Jing, S. (Frank) Liu and J. Yan, *Colloids Surf., A*, 2023, **679**, 132638.
126 M. Islam, G. Ali, M.-G. Jeong, W. Choi, K. Y. Chung and H.-G. Jung, *ACS Appl. Mater. Interfaces*, 2017, **9**, 14833–14843.
127 S. Zhang, W. Jiang, Y. Li, X. Yang, P. Sun, F. Liu, X. Yan, Y. Gao, X. Liang, J. Ma and G. Lu, *Sens. Actuators, B*, 2019, **291**, 266–274.
128 M. Alharthy, M. H. Suliman, A.-R. Al-Betar, Y. Wang, Z. Tian, Q. A. Drmosh, Z. H. Yamani and M. Qamar, *Sustainable Energy Fuels*, 2021, **5**, 2704–2714.
129 P. V. Shinde, P. Mane, B. Chakraborty and C. Sekhar Rout, *J. Colloid Interface Sci.*, 2021, **602**, 232–241.
130 T. Rasheed, A. Rasheed, F. M. A. Alzahrani, S. Ajmal, M. F. Warsi, M. S. Al-Buriahi, G. Dastgeer and S. G. Lee, *Fuel*, 2023, **346**, 128305.
131 P. Asen, A. Esfandiar and H. Mehdipour, *Nanoscale*, 2022, **14**, 1347–1362.
132 S. Ghorbanzadeh, S. A. Hosseini and M. Alishahi, *J. Alloys Compd.*, 2022, **920**, 165811.
133 H. Huang, B. Shen, M. Yan, H. He, L. Yang, Q. Jiang and G. Ying, *Fuel*, 2022, **328**, 125234.
134 C. E. Park, R. A. Senthil, G. H. Jeong and M. Y. Choi, *Small*, 2023, **19**(27), 2207820.
135 J. Li, X. Wang, C. Chen, Q. Li, Z. Chen, H. Guo, X. Lv and J. Dang, *Appl. Catal., B*, 2025, **377**, 125494.
136 X. Li, H. He, Y. Yu, Z. Wang, R. Zheng, H. Sun, Y. Liu and D. Wang, *Appl. Surf. Sci.*, 2024, **645**, 158838.
137 N. H. Attanayake, S. C. Abeyweera, A. C. Thenuwara, B. Anasori, Y. Gogotsi, Y. Sun and D. R. Strongin, *J. Mater. Chem. A*, 2018, **6**, 16882–16889.
138 L. Huang, L. Ai, M. Wang, J. Jiang and S. Wang, *Int. J. Hydrogen Energy*, 2019, **44**, 965–976.
139 X. Wu, Z. Wang, M. Yu, L. Xiu and J. Qiu, *Adv. Mater.*, 2017, **29**, 1–8.
140 J. Liu, Y. Liu, D. Xu, Y. Zhu, W. Peng, Y. Li, F. Zhang and X. Fan, *Appl. Catal., B*, 2019, **241**, 89–94.
141 L. Chen, J. Liang, Q. Zhang, X. Hu, W. Peng, Y. Li, F. Zhang and X. Fan, *Int. J. Hydrogen Energy*, 2022, **47**, 10583–10593.
142 C. Yelgel, Ö. C. Yelgel and O. Gülseren, *J. Appl. Phys.*, 2017, **122**, 065303.
143 S. Han, Y. Chen, Y. Hao, Y. Xie, D. Xie, Y. Chen, Y. Xiong, Z. He, F. Hu, L. Li, J. Zhu and S. Peng, *Sci. China Mater.*, 2021, **64**, 1127–1138.
144 B. Sarfraz, M. T. Mehran, F. Shahzad, S. Hussain, S. R. Naqvi, H. A. Khan and K. Mahmood, *RSC Adv.*, 2023, **13**, 22017–22028.
145 L. Tie, N. Li, C. Yu, Y. Liu, S. Yang, H. Chen, S. Dong, J. Sun, S. Dou and J. Sun, *ACS Appl. Energy Mater.*, 2019, **2**, 6931–6938.

146 Z. He, Z. Tan, Y. Pu, Q. Li, W. Hong, R. Li and X. Gou, *J. Solid State Chem.*, 2023, **327**, 124264.
147 N. Li, Y. Zhang, M. Jia, X. Lv, X. Li, R. Li, X. Ding, Y.-Z. Zheng and X. Tao, *Electrochim. Acta*, 2019, **326**, 134976.
148 H. Zong, K. Yu and Z. Zhu, *Electrochim. Acta*, 2020, **353**, 136598.
149 N. C. S. Selvam, J. Lee, G. H. Choi, M. J. Oh, S. Xu, B. Lim and P. J. Yoo, *J. Mater. Chem. A*, 2019, **7**, 27383–27393.
150 A. Patra, R. Samal and C. S. Rout, *Catal. Today*, 2023, **424**, 113853.
151 H. Jiang, Z. Wang, Q. Yang, L. Tan, L. Dong and M. Dong, *Nano-Micro Lett.*, 2019, **11**, 1–14.
152 P. Zhang, Z. Wang, L. Liu, L. H. Klausen, Y. Wang, J. Mi and M. Dong, *Appl. Mater. Today*, 2019, **14**, 151–158.
153 K. Chaudhary, B. Basha, S. Zulfiqar, S. Yousaf, E. W. Cochran, M. S. Al-Buriahi, M. Farooq Warsi and M. Shahid, *Fuel*, 2023, **351**, 128856.
154 R. Samal, C. Debbarma and C. S. Rout, *Catal. Today*, 2023, **424**, 113880.